Moisture Budget Estimates Derived from Airborne Observations in an Arctic Atmospheric River During its Dissipation

Henning Dorff[1,2], Florian Ewald[3], Heike Konow[4,1], Mario Mech[5], Davide Ori[5], Vera Schemann[5], Andreas Walbröl[5], Manfred Wendisch[6], and Felix Ament[1,4]

[1]Meteorological Institute, University of Hamburg, Hamburg, Germany
[2]International Max Planck Research School on Earth System Modelling, Max Planck Institute for Meteorology, Hamburg, Germany
[3]Deutsches Zentrum für Luft- und Raumfahrt, Institut für Physik der Atmosphäre, Oberpfaffenhofen, Germany
[4]Max Planck Institute for Meteorology, Hamburg, Germany
[5]Institute of Geophysics and Meteorology, University of Cologne, Cologne, Germany
[6]Leipzig Institute for Meteorology, Leipzig University, Leipzig, Germany

Correspondence: Henning Dorff (henning.dorff@uni-hamburg.de)

Abstract. This study quantifies the evolution of the moisture budget components of an Arctic atmospheric river (AR) derived from airborne observations from two research flights on consecutive days. We investigate how the poleward transport of warm and moist air masses by ARs generates precipitation near the sea ice edge, and how advection and evaporation additionally affect the local moisture amount during the dissipation phase of the AR.

5   Using the High Altitude and LOng Range Research Aircraft (HALO), we derive the atmospheric moisture budget components (local tendency of moisture, evaporation, moisture transport divergence and precipitation) within an intense Arctic AR event during the HALO–$(\mathcal{AC})^3$ aircraft campaign. The components are quantified in sectors ahead of the AR-embedded cold front by airborne observations from dropsondes, radiometers and a radar. They are compared with model-based values from reanalyses and numerical weather prediction simulations.

10   The observational moisture budget components in the pre-cold frontal sectors contribute up to $\pm\,1\,\mathrm{mm\,h^{-1}}$ to the local moisture amount. The moisture transport divergence primarily controls the local moisture amount within the AR, while surface interactions are of minor importance. Precipitation is heterogenous but overall weak ($<0.1\,\mathrm{mm\,h^{-1}}$) and evaporation is small. Although the AR decreases in strength, the budget components change from drying to significant moistening, mainly due to moisture advection. For this AR, we demonstrate the feasibility of the budget closure using single aircraft measurements, although we find significant residuals. Model-based comparisons suggest that these residuals stem from grid sub-scale variability within the AR corridor.

1 Introduction

The rapid increase in surface temperature in the Arctic over recent decades is, together with the strong decrease in Arctic sea ice cover and thickness, one of the most striking consequences of a multitude of intertwined processes and feedback
20 mechanisms within the Arctic climate system (Rantanen et al., 2022; Wendisch et al., 2023), consolidated by the term of Arctic

Amplification (Serreze and Francis, 2006). One of the coupled mechanisms contributing to Arctic Amplification concerns the large-scale meridional air mass transport, which appears for exchanging the Arctic with mid-latitude and subtropical/tropical air masses (Pithan et al., 2018; Wendisch et al., 2021). Poleward air mass transport into the Arctic is associated with warm and moist air masses (Dufour et al., 2016; Woods and Caballero, 2016). Future climate projections indicate an increase in poleward
25   moisture transport, which would intensify evaporation and precipitation (Bintanja et al., 2020).

Poleward moisture transport is realised by so-called warm air intrusions, which, if constrained within narrow and elongated water vapour-rich filaments, occur as atmospheric rivers (ARs; Zhu and Newell, 1998). Nash et al. (2018) quantified the contribution of ARs to the total poleward moisture transport to the Arctic at about 70 %. Arctic climate simulations by Kolbe et al. (2023) suggest that enhanced poleward moisture transport in a future warmer climate is almost entirely due to ARs. Zhang
30   et al. (2023) report that the rising frequency of Arctic ARs intensifies the sea ice losses. In turn, the response of ARs to Arctic sea ice loss is debated (Ma et al., 2021). These discussions motivate the need to elucidate the physical processes in the ARs and their interaction with the prevailing cold and dry Arctic air masses and sea surface types.

On synoptic timescales, the presence of ARs can trigger significant warming in Arctic regions (e.g. Neff et al., 2014), leading to substantial sea ice loss (Woods and Caballero, 2016) and melting of the Greenland ice sheet (Mattingly et al., 2018; Neff,
35   2018). In addition to induced surface heating (Woods and Caballero, 2016; You et al., 2022), liquid precipitation related to ARs essentially promotes the melting (Mattingly et al., 2018; Viceto et al., 2022). Lauer et al. (2023) identified ARs as one of the main contributors to total Arctic precipitation, with the North Atlantic as a major moisture uptake region (Vázquez et al., 2018). Poleward extratropical cyclones and embedded warm conveyor belts support the meridional propagation of moist air masses ahead of the cold front towards the Arctic Ocean and thus the formation of ARs reaching the Arctic sea ice region (e.g.
40   Dacre et al., 2019; Papritz et al., 2021). You et al. (2022) found that the moist and warm air masses of ARs undergo substantial air mass transformations along their meridional transport, while the transformations tend to intensify as they cross the sea ice (Komatsu et al., 2018).

To elucidate the transformation processes of moisture in the Arctic ARs, we need to unravel the specific moisture budget components. Seager and Henderson (2013) highlight that the divergence of the integrated water vapour transport ($\boldsymbol{IVT}$) links
45   the temporal evolution of local moisture amount to precipitation amount. Dorff et al. (2024) extracted the role of horizontal moisture advection across the AR-embedded front as a major contributor to $\boldsymbol{IVT}$ divergence in the Arctic ARs. Nygård et al. (2020) find that horizontal moisture transport and its advection dominate the regional moisture patterns in the Arctic. However, this dominance of advection has to be seen in relation to the tendency of AR-related precipitation (Viceto et al., 2022; Lauer et al., 2023). Guan et al. (2020) diagnose that AR precipitation strongly correlates with air mass convergence rather than
50   advection. Therefore, the different contributions need to be discussed for further verification, including all components of the moisture budget, for which in particular the spatial variability within ARs needs to be resolved.

High-resolution observations of $\boldsymbol{IVT}$ divergence have not yet been collected for the Arctic. One reason for this lack is the remote and sporadic occurrence of Arctic ARs over the Arctic Ocean, where no dense observational networks are available. Also, quantifying moisture transport requires simultaneous measurements of winds and moisture throughout the entire
55   troposphere. Satellites can estimate the spatial distribution of the integrated water vapour (IWV) but have difficulty profiling

water vapour and winds in the lower troposphere. The radiosonde network presented in Nygård et al. (2020) is too coarse to sufficiently resolve the strong moisture transport gradients that exist along AR cross-sections perpendicular to the transport direction (Guan and Waliser, 2015; Ralph et al., 2017), as reanalyses have also identified in the Arctic (Dorff et al., 2024). These gradients cause differences in IVT divergence across the AR cross-section (Guan et al., 2020; Dorff et al., 2024).

60 Furthermore, the validation of the previous reanalysis-based results with observations is still lacking for the Arctic. Similarly, observations of precipitation and evaporation over the Arctic Ocean are sparse and mostly based on drifting buoys (Barrett et al., 2020). These limitations prevent a reliable establishment of moisture budget components within individual ARs.

Long-range research aircraft provide new perspectives for analysing the moisture budget components in ARs. Dropsonde releases from aircraft provide comprehensive data on vertical moisture and wind profiles. Aircraft equipped with a remote

65 sensing configuration, such as the High Altitude and LOng Range research aircraft (HALO; Stevens et al., 2019), also enable precipitation measurements. Previous airborne measurements, using the NOAA Gulfstream IV research aircraft, have provided observational data of AR moisture budget components (Neiman et al., 2014), reaching to the closure of the budget for mid-latitude ARs (Norris et al., 2020). The airborne precipitation rates in Norris et al. (2020) were estimated by applying radar reflectivity (Z) and rain rate (R) relationships derived from shipborne observations within the AR. Yet, the application of

70 various measurement platforms is associated with expensive costs. For IVT divergence purposes, Norris et al. (2020) released dropsondes over horizontally extended areas across the AR to capture the expected differences along the AR transect, as noted by Cobb et al. (2021a). However, their budget regions were too small to cover the full AR cross-section variability in the budget components, as suggested by Guan et al. (2020). For the observational moisture budget closure, Norris et al. (2020) combined the airborne observations with spaceborne IWV. In turn, for Arctic conditions, Vaquero-Martínez et al. (2020) summarise

75 numerous spaceborne platforms to underestimate high IWV, especially in cloudy conditions and under large solar zenith angle, which are ubiquitous in Arctic ARs. Crewell et al. (2021) confirms that spaceborne IWV is less reliable in Arctic ARs.

To fill the gap of moisture observations in the Arctic ARs, the HALO–$(\mathcal{AC})^3$ aircraft campaign was performed in March and April 2022 (Wendisch et al., 2024). HALO observed air mass transformations in meridional atmospheric transports over the North Atlantic and Arctic Ocean in a six-week observation period over the open ocean and the marginal and closed sea ice. The

80 first campaign week was characterised by a series of ARs, propagating across the North Atlantic towards the Arctic (Walbröl et al., 2024). Special flight patterns were designed to sample enclosed AR subregions. We consider this data to address our first pioneering research goal of this study: *To derive all moisture budget components in Arctic ARs from a research aircraft (G1).*

Investigating the temporal evolution of AR moisture characteristics is fundamental for understanding the air mass transformations that occur in ARs. However, the spatio-temporal tracking of AR characteristics has primarily relied on simulations

85 (Guan and Waliser, 2019; Kirbus et al., 2023). In the Arctic, ARs are typically found in the termination phase of their life cycle (Guan and Waliser, 2019). During HALO–$(\mathcal{AC})^3$, we observed an intense AR event sampled by HALO over two consecutive days (March 15 and 16, 2022). Over this period, the AR experienced a significant decrease in intensity (quantified by IVT) and dissipated considerably. Using the airborne AR moisture budget representation, we have analysed this transition *to examine how the moisture budget components evolve during the dissipation phase of the AR*, the second goal of our study (G2).

The observationally determined budget components are tainted with uncertainties. As shown in Norris et al. (2020), the uncertainties are not negligible; they must be quantified to interpret the budget components and the emerging residuals. Furthermore, the airborne moisture budget estimates refer to a rather large area that is sampled by a single curtain along the flight path. Assessing the representativeness of the airborne results for entire AR sectors further improves the uncertainty analysis of previous studies. Norris et al. (2020) and Dorff et al. (2024) conclude that the nonstationarity of ARs during the flight leads to significant deviations in the budget components. Still, they examined the spatial representativeness to a lesser extent. To mitigate this issue, we conduct a model-observation comparison. We utilize the model grid data to mimic and explain potential effects that can influence the budget components based on the airborne perspective in order *to assess how accurate and representative the airborne budget components are for the entire AR flight corridor (G3)*.

To cover the three research goals, the manuscript is structured as follows: Section 2 introduces HALO observing ARs during HALO–$(\mathcal{AC})^3$ and the instrumentation to derive the moisture budget components, the model configuration and synoptic conditions for the AR over the two flight days. Section 3 specifies the airborne derivation of the budget components (G1). Section 4 examines the evolution of the moisture budget components over time (G2). Using the model-based representation, Sect. 5 assesses the plausibility and representativeness of the airborne curtain measurements for the AR corridors (G3). Our conclusions synopsise potential strategies to further elucidate moisture transformations in the Arctic ARs using airborne observations.

2 Atmospheric river data from HALO–$(\mathcal{AC})^3$

The airborne observations used in this study were gathered during the six-week HALO-$(\mathcal{AC})^3$ aircraft campaign (Wendisch et al., 2024), which was conducted in March and April 2022 using three research aircraft (Ehrlich et al., 2024). Besides the low-flying research aircraft Polar 5 and Polar 6 (Wesche et al., 2016), HALO, a modified Gulfstream G550, was used for long-range observations, allowing flight durations of over 8 h, with a cruising speed of around $250\,\mathrm{m\,s^{-1}}$. Flight altitudes above 12 km enable combined in situ and remote-sensing measurements throughout the troposphere. The instrumentation was aligned with previous remote sensing configurations (Stevens et al., 2019; Konow et al., 2021). HALO was based in Kiruna (Sweden) and flew over the North Atlantic and Arctic Ocean to follow Arctic air masses within mesoscale meridional transport patterns.

2.1 Airborne measurement data used from HALO

From the cloud observatory configuration aboard HALO (Konow et al., 2021; Ehrlich et al., 2024), we use and introduce below two instrument packages providing remote-sensing and in-situ measurements to derive the moisture budget components. First, we use measurements of the HALO Microwave Package (HAMP, Mech et al., 2014), which consists of two nadir instruments: a Ka-band cloud radar measuring at 35 GHz and a suite of passive microwave radiometers with 26 frequencies from the K-band (22.24 to 31.4 GHz), the V-band (50.3 to 58 GHz), at the W window (90 GHz), the F-band (118.75 ± 8.5 GHz) and the G-band (183.31 ± 7.5 GHz). The 195.81 GHz channel was not operated during HALO-$(\mathcal{AC})^3$. Here, we utilize the unified HAMP dataset published by Dorff et al. (2023), which is based on the unification by Konow et al. (2019). The data of the two instruments are synchronised to a collocated 1 s temporal resolution. The time series of brightness temperatures (T_b) from the

radiometer channels were synchronised with the equivalent radar reflectivity factor and linear depolarisation ratio. The nadir radar range gates were interpolated onto a vertical grid of 30 m resolution. The radar reflectivities and the radiometer brightness temperatures were post-calibrated, quality checked and supplemented with a corresponding surface mask that distinguishes

125 between land, sea and sea ice cover (Ehrlich et al., 2024).

Second, vertical profiles of moisture and wind were measured by dropsondes, from which the moisture transport can be derived. The sondes deployed from HALO are of the Vaisala RD-41 type (Vaisala, 2020; George et al., 2021). During their descent, the sondes simultaneously measure relative humidity and wind speed with an accuracy of 1 % and $0.1\,\mathrm{m\,s^{-1}}$, respectively (Konow et al., 2019). In our analysis, we include the sonde measurements in a processing state equivalent to the Level 2

130 data in George et al. (2021), which have undergone quality checks after processing with the Atmospheric Sounding Processing ENvironment (ASPEN, 2024). The Global Telecommunication System (GTS) has partly adopted the sonde measurements in the model assimilation of operational Numerical Weather Prediction (NWP).

2.2 Model data

We consider two model configurations to compare the airborne observations with model results. First, the global ECMWF

135 Reanalysis v5 (ERA5; Hersbach et al., 2020) is used to investigate Arctic AR conditions. ERA5 data fields have a vertical resolution of 137 model levels and a horizontal grid spacing of $0.25° \times 0.25°$. For the Fram Strait and the Greenland Sea, the ERA5 latitude-longitude grid results in spacings of about 30 km. Cobb et al. (2021b) find that ERA5 outperforms other global reanalyses regarding AR characteristics. Furthermore, recent studies emphasise the high performance of ERA5 for Arctic conditions (e.g. Graham et al., 2019; Wu et al., 2023). This justifies the extended use of ERA5 to study AR conditions,

140 especially in the Arctic (Fearon et al., 2021; Zhang et al., 2022; Lauer et al., 2023). The dropsonde data could not be included in the assimilation phase of ERA5 during the AR event of this study (Ehrlich et al., 2024) and thus, it is appropriate to compare ERA5 data with the independent dropsonde measurements.

Second, we include the AR representation by forecasts from the ICOsahedral Nonhydrostatic numerical weather prediction model (ICON; Zängl et al., 2014). The modelling system of ICON is suitable for global and limited-area applications (Dipankar

145 et al., 2015). We consider a modified and non-operational ICON limited area mode with a nominal horizontal resolution of about 2.4 km, similar to Schemann and Ebell (2020), which we refer to as ICON-2km. The ICON-2km domain extends from 70 to 85°N and from -20 to 30 °E. ICON-2km is initialised at 00 UTC of every day. The lateral boundary conditions in ICON-2km are obtained by one-way nesting using the output of the operational ICON global model in a horizontal resolution of 13 km (Zängl et al., 2014). ICON-2km is run for a forecast time of 48 h with the atmospheric state saved every 30 minutes. The cloud

150 microphysics is represented by five hydrometeor classes in a one-moment bulk scheme similar to Lin et al. (1983). Vertical data in ICON-2km are given for 150 terrain-following height levels. In a similar model configuration, Bresson et al. (2022) reported on the skilful ability of high-resolution ICON limited-area modes in the AR representation at deca-kilometre scales against ERA5. The 30-minute output of ICON-2km captures the displacement of AR filaments better than the hourly ERA5 output. Following Dorff et al. (2024), we interpolate ERA5 and ICON-2km onto the flight track in space and time to compare

155 their representation with the airborne values and among each other.
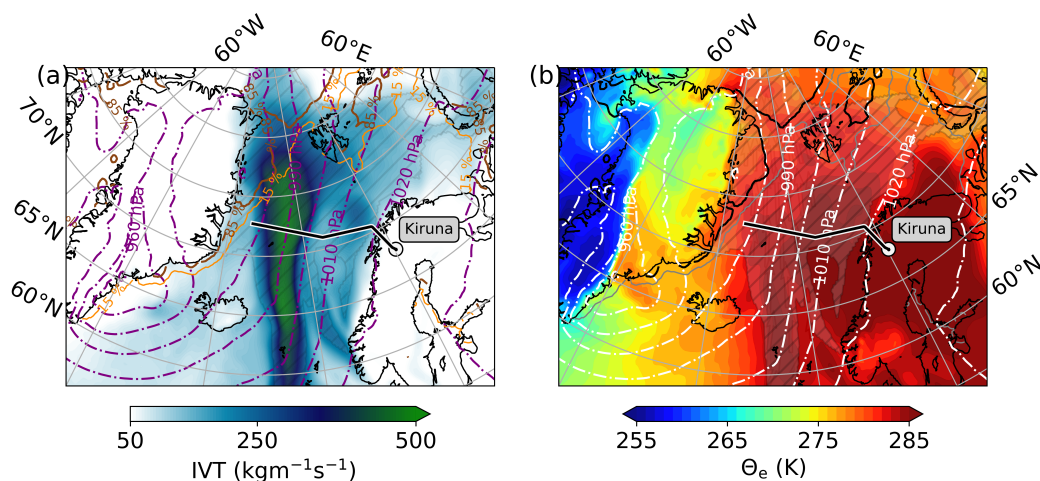
Figure 1. Synoptic ERA5-based overview of the AR event on March 15, 2022, 11 UTC, when HALO departed from Kiruna and crossed the AR for the first time (black-white bold line). Grey hatches show the AR boundaries according to the AR catalogue of Lauer et al. (2023). a) shows contours of the magnitude of IVT, b) the pseudo-equivalent potential temperature (Θ_e) at the 850 hPa level. Surface isobars are given in purple (a) and white (b) contour lines. Sea-ice fractions above 0.15 and 0.85 are shown as brownish lines in a) and greyish in b).

2.3 Arctic Atmospheric River event

The meteorological conditions during the first week of HALO-$(\mathcal{AC})^3$ (mid of March 2022) were characterised by a sequence of warm and moist air intrusions, some of which met the criteria for ARs in terms of intensity of moisture transport and geometric extent. Walbröl et al. (2024) showed that these ARs were quite strong for Arctic conditions and entered the Arctic via typical

160 paths along the North Atlantic, steering towards the Fram Strait and Barents Sea, before partially reaching the Arctic Ocean.

In this case study, we focus on the strongest AR event of HALO-$(\mathcal{AC})^3$, which entered our region of interest (Greenland Sea and Fram Strait) on 15 March 2022, sampled during research flight 05 (RF05, Fig. 1). Walbröl et al. (2024) classify this AR as a very strong event for Arctic conditions. Here, we describe the synoptic conditions causing the AR and its temporal evolution towards the following day, when the AR was observed by a subsequent research flight (RF06).

165 ### 2.3.1 Synoptic conditions

A preceding rapid cyclogenesis led to a "bomb" cyclone (air pressure drop greater than $24\,\mathrm{hPa\,d}^{-1}$, as defined in Sanders and Gyakum, 1980) in southern Greenland. Between the Norwegian Sea and Greenland Sea, the intense steering low and a Scandinavian ridge of high pressure created strong zonal pressure gradients, featuring a dominantly meridional circulation (Walbröl et al., 2024). On 15 March 2022 (RF05), the cyclone exhibited a core air pressure $< 960\,\mathrm{hPa}$ off the coast of the Denmark

170 Strait, while high air pressure above $1020\,\mathrm{hPa}$ prevailed over Scandinavia (Fig. 1). The meridional circulation advected moist
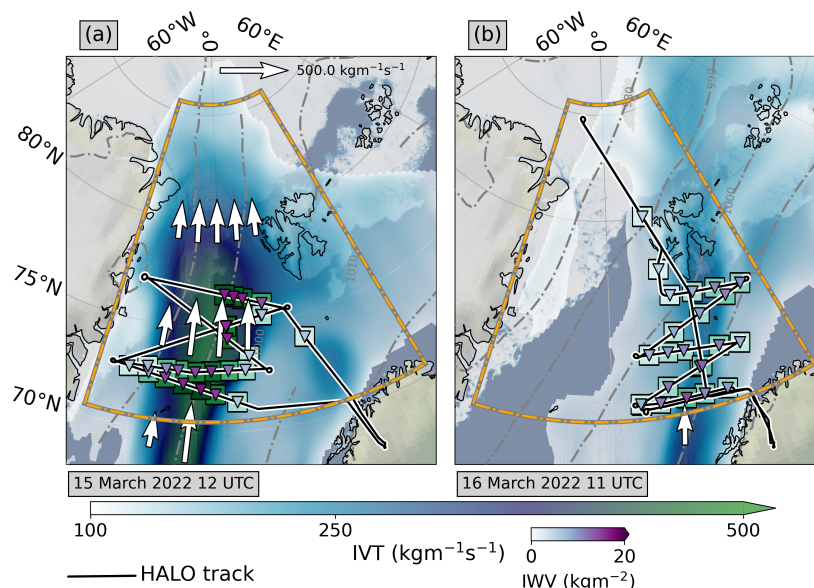
Figure 2. ERA5-IVT contours for (a) 15th and (b) 16th March 2022 of the AR, consecutively sampled by HALO. Coloured squares (triangles) indicate dropsonde values of IVT and IWV. Grey contour lines depict the surface pressure isobars. Sea-ice maps are based on the AMSR-2 sea ice product provided by the University of Bremen (Spreen et al., 2008). The orange quadrangle represents the ICON-2km model domain.

(Fig. 1a) and warm (Fig. 1b) air masses poleward over the Greenland Sea, leading to exceptional air mass conditions in this region (Walbröl et al., 2024), with IVT up to $500\,\mathrm{kg\,m^{-1}\,s^{-1}}$ over large areas along the AR in northward orientation (Fig. 1a).

The AR crossed the marginal sea ice zone and sea ice edge from the Denmark Strait towards the northern tip of Svalbard. Horizontally compressed isobars indicate strong winds driving the intense horizontal transport. This moisture transport was
175   associated with very warm air masses according to the 850 hPa pseudo-equivalent potential temperature Θ_e (Fig. 1b), causing record warming in the Arctic. Θ_e exceeded $285\,\mathrm{K}$ over a large extent from the AR along the $0°$ meridian to Scandinavia. The meridional flow thus causes a strong advection of warm and moist air. Over Central Greenland, the latent warming was less pronounced, with $\Theta_e \leq 270\,\mathrm{K}$ and a cold western coast of Greenland with $\Theta_e \leq 260\,\mathrm{K}$. While the majority of the AR is located in air masses with $\Theta_e \geq 280\,\mathrm{K}$), the western AR flank behind the AR propagation showed strong gradients. They indicate the
180   presence of a cold front favouring the intrusion of moderately colder and drier air masses to the west of the AR.

2.3.2   Evolution of the atmospheric river

HALO sampled the AR on two consecutive days (Fig. 2), during which the AR propagated north-eastward, with its eastern flank west of Svalbard during RF05 and east of it during RF06, before approaching the Norwegian coast with its southern end. While the AR reached its maximum intensity before both RFs (Walbröl et al., 2024), HALO observed the AR during its dissipation
185   north of $70°$, within the ICON-2km model domain. During RF05 (Fig. 2a), IVT values still reached up to $500\,\mathrm{kg\,m^{-1}\,s^{-1}}$, while IVT dropped below $300\,\mathrm{kg\,m^{-1}\,s^{-1}}$ during RF06 (Fig. 2b). One reason for the decay of the AR is the reduction of the

horizontal pressure gradients, which decelerates the winds. The IWV from dropsonde observations (Fig. 2) shows that the atmosphere became drier within the AR. South of the RF06 flight path, an intensification of moisture transport was identified, which is attributed to orographic convergence. Based on the ERA5 AR catalogue (Lauer et al., 2023), the dissipation of the AR resulted in the moisture transport filaments no longer being classified as AR during RF06 (Fig. 2b). Still, the moisture transport remained high enough to be classified as AR for Arctic conditions but in a too-narrow and disturbed flow.

RF05 and RF06 sampled different air masses of the AR. While RF05 captured the AR between its centre and the exit region, RF06 is located in the entrance region. The planned matching of same air masses on consecutive days, one of the HALO–$(\mathcal{AC})^3$ objectives (Wendisch et al., 2024), could not be achieved for both flights due to Air Traffic Control (ATC) restrictions.

3 Estimation of moisture budget components using airborne observations

The atmospheric moisture budget is the major framework of this study to investigate the transformation of moisture in the Arctic AR. In a vertically integrated perspective, the moisture budget components are defined as:

$$
\underbrace{\frac{\delta IWV}{\delta t}}_{\text{Local Change in Integrated Water Vapour}} = \underbrace{E}_{\text{Evaporation}} - \underbrace{P}_{\text{Precipitation}} - \underbrace{\boldsymbol{\nabla} \cdot \boldsymbol{IVT}}_{\text{Horizontal divergence of Integrated Water Vapour Transport}} + \underbrace{\epsilon}_{\text{Residual}}, \tag{1}
$$

with all components in kilograms per metre squared per second. Precipitation and evaporation refer to surface values, while the integrated water vapour IWV and integrated water vapour transport $\boldsymbol{IVT}$ are vertical integrals defined as:

$$
IWV = -\frac{1}{g} \int_{p_{\text{sfc}}}^{p_{\text{top}}} q \, \mathrm{d}p, \tag{2}
$$

$$
\boldsymbol{IVT} = -\frac{1}{g} \int_{p_{\text{sfc}}}^{p_{\text{top}}} q\boldsymbol{V} \, \mathrm{d}p, \tag{3}
$$

where g is the gravitational acceleration. q is the specific humidity and $\boldsymbol{V}$ the horizontal wind vector, both vertically-integrated over the pressure (p) range from the surface (p_{sfc}) to the top of the troposphere (p_{top}). When we provide IVT values, we mean its magnitude. Equation 1 is not necessarily closed from observations (i.e., the left-hand side is not equal to the physical processes on the right-hand side), as each component is derived independently, so a residual ϵ may need to be added to achieve equality. Furthermore, ϵ can include secondary processes, such as the moisture flux through a tilted pressure surface, as described by Seager and Henderson (2013), which, however, is overall minor in ARs (Guan et al., 2020). Another process is the contribution of cloud condensate, but it is up to two orders of magnitude smaller than water vapour. The divergence of moisture transport affects the moisture budget in two ways, which we can attribute by splitting $\nabla \cdot IVT$ into:

$$
\boldsymbol{\nabla} \cdot \boldsymbol{IVT} = -\frac{1}{g} \int_{p_{\text{sfc}}}^{p_{\text{top}}} \boldsymbol{\nabla} \cdot (q\mathbf{V}) \, \mathrm{d}p = -\frac{1}{g} \int_{p_{\text{sfc}}}^{p_{\text{top}}} \underbrace{q \left(\boldsymbol{\nabla} \cdot \mathbf{V} \right)}_{\text{Mass divergence } (DIV_{\text{mass}})} \mathrm{d}p + \frac{1}{g} \cdot \int_{p_{\text{sfc}}}^{p_{\text{top}}} \underbrace{\mathbf{V} \cdot (-\nabla q)}_{\text{Horizontal moisture advection } (\text{ADV}_{\text{q}})} \mathrm{d}p. \tag{4}
$$
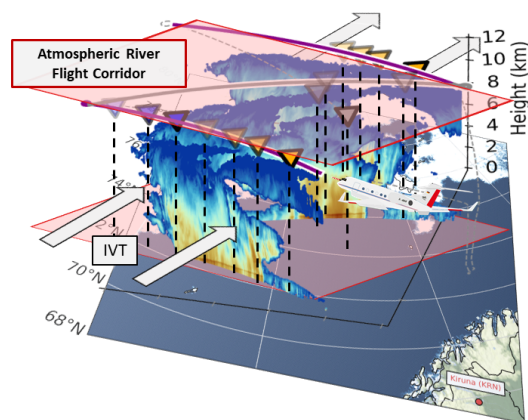
Figure 3. Realisation of a zigzag flight pattern during RF05 to derive the moisture budget components inside an Arctic AR flight corridor. The surface map with the sea-ice extent, as in Fig. 2, is superimposed with the vertical radar reflectivity curtain. Boundary flight legs (purple) quantify the in- and outgoing IVT via dropsondes (triangles), while the internal leg (grey) samples precipitation, evaporation and IWV inside the AR flight corridor. Pre-frontal (post-frontal) dropsonde releases are indicated by orange (purple) triangles, internal ones are grey.

The first term on the right side of Eq. 4 represents the dynamical mass divergence, which is the product of specific humidity and horizontal divergence. The mass divergence can be related to vertical velocity via the continuity equation and is closely

215 linked to precipitation (Wong et al., 2016; Norris et al., 2020). The right side's second term of Eq. 4 represents the horizontal advection of moisture that Guan et al. (2020) show to be little correlated to precipitation formation. Instead, it locally affects the amount of water vapour. We define the vertically integrated decompositions in Eq. 4 as $IDIV_{\mathrm{mass}}$ and $IADV_{\mathrm{q}}$, respectively.

3.1 Flight patterns and categorisation of atmospheric river sectors

For the airborne derivation of all components of the moisture budget, our first research goal (G1, Sect. 1), flight patterns

220 must sample areas of the AR in a specific way. Flight tracks that enclose areas, such as circles, are often used to calculate the mesoscale horizontal divergence (e.g. Bony and Stevens, 2019; Paulus et al., 2024). However, if a single circle is placed across the entire lateral width of the AR, the heterogeneities of moisture and wind fields in the AR across the embedded cold front would be smoothed out (Cobb et al., 2021a; Dorff et al., 2024). The high lateral variability in the moisture transport characteristics of ARs requires long flight legs across the AR. Therefore, Neiman et al. (2016) and Norris et al. (2020) focused

225 their enclosing flight patterns more on the AR transect to capture this cross-sectional variability. However, their patterns were too small to cover the lateral variability of the budget components identified by Guan et al. (2020) from reanalyses.

Dorff et al. (2024) recommend full cross-sections of the AR. An internal flight leg shall connect two parallel cross-sections, resulting in a zigzag flight pattern. Figure 3 shows the realisation of the zigzag pattern for an AR flight corridor during RF05. The zigzag pattern samples the AR transverse to the IVT direction. The boundary cross-section legs perpendicular to the

230 main flow (Fig. 3) quantify the inflow and outflow of the flight corridor, i.e. ingoing and outgoing IVT across the lateral AR

extension. Dropsondes densely sample both cross-sections to derive $\nabla \cdot IVT$. The internal legs explore the precipitation rate, evaporation and the water load within the AR flight corridor. The radar reflectivities in Fig. 3 show very deep clouds in the AR for Arctic conditions. The cloud top height is up to 12 km. Significant radar echoes down to the surface were recorded in the AR core (middle of the cross-sections). The high reflectivity band at about 1-2 km height (Fig. 3), a so-called bright band, indicates a melting layer. Bright bands result from snowflakes coated by liquid water, causing higher radar reflectivities (Gray et al., 2001). Below, liquid precipitation can be expected.

We divide sectors along the lateral AR cross-sections, similar to the approach suggested by Guan et al. (2020). This distinction considers the presence of a cold front embedded in ARs (Ralph et al., 2004), whereby different thermodynamic conditions prevail on both sides of the front. Guan et al. (2020) calculate the moisture budget across the main AR axis and the embedded front and report on significant differences in the budget components across the AR (front). For our AR, the gradients of θ_e (Fig. 1b) suggest remnants of a cold front. We thus divide the AR flight corridors into eastern and western parts. Concerning the approximate location of the cold front, we refer to the eastern (western) half as the pre-frontal (post-frontal) sector.

Note that recent studies (Guan et al., 2020; Cobb et al., 2021a; Dorff et al., 2024) categorise ARs into three sectors, with the AR core as a separate one between the pre- and post-frontal sectors, containing IVT values $\geq 80\%$ of the maximum IVT. However, given the nature of the irregular sonde spacing and the purpose of including as many sondes as possible in the sector-based divergence calculations, we assign the sondes released in the eastern part of the AR core to our pre-frontal sector and those in the western part to the post-frontal sector. We also restrict the extent of our sector to the actual positions of the outer sonde releases. This two-sector separation is shown in Fig. 3 by the orange sondes referring to the pre-frontal sector.

During RF05, ATC restrictions in Danish airspace that extends over the western regions of the AR flight corridors did not allow sonde releases in the post-frontal sector for the northern cross-sections (Fig. 3). This lack of data prevents reliable sonde-based divergence estimates for the post-frontal sectors. Hence, the subsequent analysis is confined to pre-frontal AR sectors. The upcoming sections refer to the pre-frontal sector that is spanned by the orange sondes in Fig. 3, henceforth denoted as S1, to demonstrate the derivation of each moisture budget component as per Eq. 1 using HALO.

3.2 Local change of integrated water vapour ($\delta IWV / \delta t$) from radiometer

The IWV is most accurately determined using dropsonde measurements of moisture profiles. However, these dropsonde profiles have limited spatial coverage. The few internal profiles may thus lack spatial representativeness for estimating the local change of IWV within the pre-frontal AR sector. To address this issue, we use the quasi-continuous HAMP radiometer measurements of the channels from 22 to 190.81 GHz (Sect. 2.1). Their 1 s measured brightness temperatures (T_Bs) are very sensitive to the emitted radiation from water vapour across the microwave spectrum (Jacob et al., 2019). In particular, the K-band channels of HAMP show rising T_B with increasing IWV. Furthermore, continuum water vapour absorption influences the T_B at window frequencies near 30 and 90 GHz.

From the observed T_B values, the IWV can be estimated using appropriate retrieval methods. We build a linear regression model retrieval, as used in Jacob et al. (2019), which we describe in Appendix A. As specified in Sect. A1, the regression coefficients between the two quantities (IWV and T_B) are based on a training dataset containing meteorological fields from
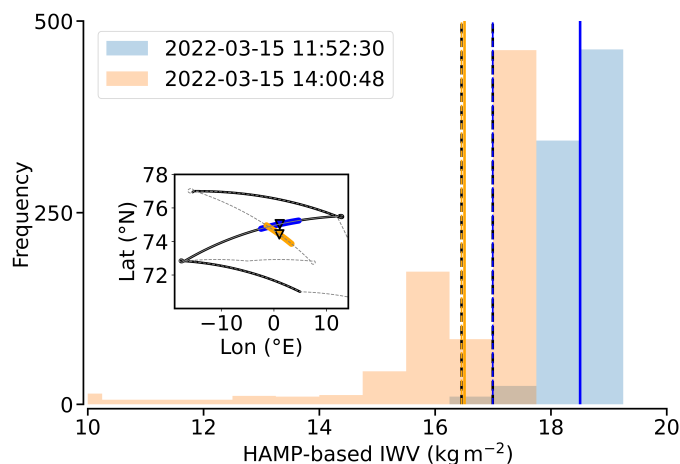
Figure 4. Determination of local change in IWV from the first sector S1 in the AR during RF05. The sub-panel demonstrates the internal flight leg segments used for estimating the change of IWV internal of S1 and two dropsonde releases (triangles) inside. Flight leg segments extend symmetrically around the sondes, whose release times are specified in the legend. For both legs, their HAMP-based IWV distribution is illustrated with their respective mean values (bold solid lines). The dashed vertical lines specify sonde-based values.

265 ECMWF Reanalysis v5 (ERA5), along with synthetic T_B generated from the Passive and Active Microwave TRAnsfer tool (PAMTRA; Mech et al., 2020). Applying the emerging retrieval coefficients to the measured T_B, the retrieved IWV data shows a good agreement with the dropsonde-based IWV over a wide range from 6–18 kg m^{-2}. Furthermore, the comparison of the airborne retrieved IWV values with the collocated and continuous ERA5-based representation confirms that the continuous HAMP representation reasonably replicates the IWV values (Sect. A2; Fig. A1).

270 To derive the local temporal changes of HAMP-retrieved IWV within the AR flight corridors, we consider the internal flight legs of the zigzag pattern (Fig. 3). The derivation of $\delta IWV/\delta t$ requires sampling a specific region at two distinct time steps. This requirement is met within the AR core at the crossing flight paths. However, the single intersection in Fig. 4 has limited representativeness for the entire sector and the internal flight legs separate from each other in the pre-frontal sectors. Therefore, we opt to compare only segments of internal flight legs that lie close to each other without considering single locations (Fig.

275 4). Symmetrically around two sonde releases, we assess the "local" change of IWV over approximately 2 hours.

While dropsonde-based IWV values in Fig. 4 differ by less than 1 kg m^{-2}, the HAMP-based mean values of each leg differ by more than 2 kg m^{-2}. The IWV distributions along the leg segments (Fig. 4) reveal a high spatial variability because we consider regions of strong IWV gradients. This variability leads to significant uncertainties in estimating local changes in IWV. To quantify these uncertainties, we subsequently extend the internal leg segments by a minute (starting from 1 and going

280 up to 10 minutes) and calculate the standard deviation of the mean local IWV change across all segments. Since the resulting uncertainties are much larger than those based on the regression retrieval, we neglect retrieval uncertainties in the uncertainty assessment of $\delta IWV/\delta t$. For the AR sector S1, we derive a value of local change of IWV of -0.79 ± 0.19 mm h^{-1}.
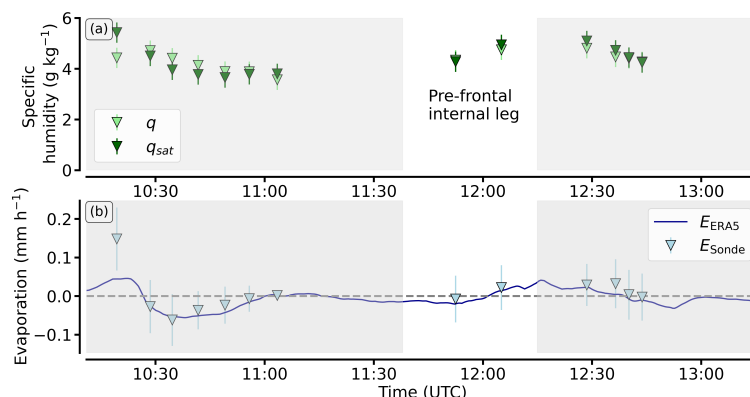
Figure 5. Dropsonde-based evaporation derivation for the first AR flight corridor of RF05. The sonde-based near-surface specific humidity and the saturation specific humidity for the given SST extracted from ERA5 are presented (a). Triangles in b) represent the sonde-based ocean evaporation resulting from the values in a). The pre-frontal segment of the internal leg relevant to S1 is highlighted (white). The continuous blue line depicts collocated ERA5-based evaporation.

3.3 Evaporation (E) estimated from dropsonde data

The surface evaporation E can be estimated from bulk approaches, taking into account surface wind, temperature and humidity.
285 Our calculations are based on the aerodynamic bulk methods of Rao et al. (1981), who derive the surface evaporation as:

$$E = c_\mathrm{d} \rho_\mathrm{a} (q_\mathrm{s} - q_\mathrm{a}) \cdot V, \tag{5}$$

where q_a is the near-surface specific humidity, q_s is the saturation specific humidity for the current sea-surface temperature (SST). ρ_a represents the air density near the sea surface. c_d is the evaporation drag coefficient, where we follow Howland and Sikdar (1983) and separate c_d for two wind regimes, with $c_\mathrm{d} = 1.4 \cdot 10^3$ for winds $\leq 14\,\mathrm{m\,s^{-1}}$ and $c_\mathrm{d} = 1.6 \cdot 10^3$ for higher
290 wind speeds V. We obtain the near-surface values from the lowest dropsonde profile levels before reaching the sea surface (below 50 m). We filter out values from heights below 0 m, as the sondes sometimes transmit data just after they enter the sea. In other cases, erroneous GPS altitude data may prevent near-surface classification, so the corresponding sondes are omitted. We calculate q_s for the SST extracted from the collocated ERA5 data. The air density is based on the near-surface sonde pressure, humidity and temperature values. Uncertainties in the derived evaporation result from Gaussian error propagation of
295 the sonde-based quantities given in Bony and Stevens (2019).

Looking at the first complete zigzag pattern that contains S1, Fig. 5a shows that sonde-based deviations between q_s and q_a are quite small, except for the first sonde. This indicates near-saturated air, with some sondes even showing super-saturated air. Sondes in supersaturation reveal small negative values in evaporation (condensation). Overall, the evaporation is weak, with absolute values below $0.05\,\mathrm{mm\,h^{-1}}$ most of the time (Fig. 5b). The uncertainties in q are much smaller than the actual values
300 of q but non-negligible (Fig. 5a). Based on the two sondes within the prefrontal internal flight segment, we calculate a mean evaporation of $0.01 \pm 0.06\,\mathrm{mm\,h^{-1}}$.

Table 1. Overview of used Z-R and Z-S relationships, categorized for radar-bands applied, how they were derived and their representativeness

Source / Label	Relationship	Band	Derivation	Representativeness
Rain				
Marshall and Palmer (1948) / MP1948	$Z = 200R^{1.6}$	S	PSD based (dyed filter papers)	stratiform precipitation (climatological)
Norris et al. (2020) / Nor2020	$Z = 466R^{1.47}$	X	PSD (shipborne disdrometer)	atmospheric rivers
Chandra et al. (2015) / Cha2015	$Z = 177R^{1.11}$	Ka	Ka-band radar & disdrometer comparison	low rain rates
Snow				
Schoger et al. (2021) / Sch2021	$Z = 77.67S^{1.22}$	Ka	airborne radar & particle probes	airborne
Matrosov (2007) / Mat2007	$Z = 56S^{1.20}$	Ka	model-based	no specification
Heymsfield et al. (2018) / Hey2018	$Z = 10.13S^{1.92}$	Ka	disdrometer PSD-based	Arctic conditions

Comparison with collocated ERA5 (Fig. 5b) verifies that the sonde-based bulk values are in a realistic order of magnitude. Moreover, ERA5 confirms the very small contribution of evaporation to the moisture budget within the AR flight corridor.

3.4 Precipitation based on radar

305 We obtain the precipitation rates by using the cloud and precipitation radar measurements from the unified dataset (Sect. 2.1; Dorff et al., 2023). These radar reflectivities are offset-calibrated following Ewald et al. (2019). In addition, we correct the reflectivities for gaseous attenuation by water vapour, which we calculate from the model of Rosenkranz (1998) using water vapour profiles from the ECMWF Integrated Forecast System (IFS) model. The conversion of radar reflectivity into precipitation rates is conventionally achieved by the application of empirically derived radar reflectivity to rain rate (Z–R)

310 relationships (e.g. Marshall and Palmer, 1948). The Z–R relationships are provided by power laws in the form of $Z = aR^b$, see Tab. 1. The parameters a and b account for variations in precipitation for a given reflectivity, arising from differences in the particle size distribution (PSD). However, the parameters vary greatly between radar frequencies, measurement viewing angles and precipitation types (Ignaccolo and De Michele, 2020). Using shipborne disdrometer data, Neiman et al. (2017) mentioned the rapid spatiotemporal evolution of drop size distributions as an AR-specific caveat to using a single Z-R relationship.

315 This dilemma is exacerbated in Arctic ARs, where the coexistence of different precipitation phases (liquid and solid) is expected. The radar bright band shown in Fig. 3 provides evidence that melting of precipitation occurs in our AR event so that we observe rain- and snowfall. The airborne estimation of precipitation rates along the internal legs for our moisture budget closure is thus twofold based on Austen (2022). This estimation requires a precipitation type classification using a melting layer detection, followed by the application of a set of multiple Z-R and reflectivity-to-snow (Z-S) relationships (Tab. 1). For

320 the precipitation type classification, we use the linear depolarisation ratio (LDR) included in Dorff et al. (2023). In the first internal flight leg, high reflectivity bands frequently occur (Fig. 6a), while the LDR represents a robust indicator for the melting layer (Fig. 6b). For the melting layer detection, Illingworth and Thompson (2011) propose an LDR threshold of -17 dB, which we apply to our radar data. The nearest-surface exceedance of the threshold marks the bright-band bottom BB_{bottom}.
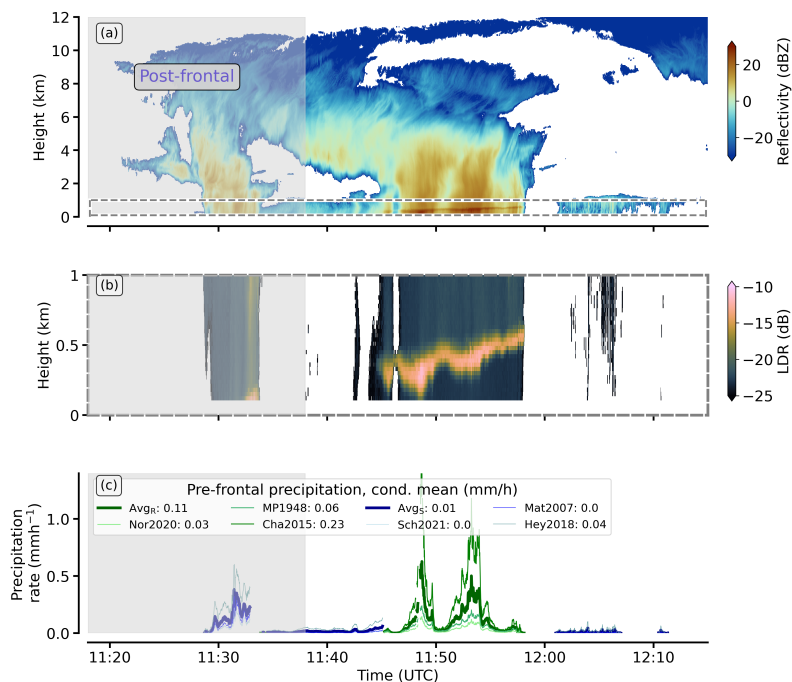
Figure 6. Radar reflectivity a), LDR b) and derived precipitation rate c) for the internal leg in the first AR corridor. The post-frontal segment is sketched in grey. The dashed rectangle in a) specifies the zoomed-in area of plotted LDR in b). Green (blue) precipitation rates in c) refer to rain (snow) rates classified by the melting layer algorithm. The legend entries in c) refer to the labels of the relationships defined in Tab. 1 and specify mean conditional precipitation rates for the pre-frontal segment of the internal flight leg and the respective relationship. Average values over all corresponding relationships are shown as bold lines for rain (Avg_R) and snow (Avg_S), respectively.

However, such a pure threshold-based melting layer detection is subject to many artefacts and outliers. Therefore, we apply additional criteria. First, the maximum BB_{bottom} height is set to 2000 m and second, its spatial gradient is restricted. We consider variations of BB_{bottom} of up to 60 m per 200 m horizontal distance as realistic. Both vertical thresholds are checked for a rolling mean window of 5 s, which is applied to the initially pure LDR-based BB_{bottom}. While the gradient threshold is very suitable for most RF legs, it is too restrictive near front regions such as those occur across ARs, where air mass transitions can cause vertical changes in the melting layer of several hundred metres in 1 km (e.g. Fig. 6b; 11:48). For this reason, we add gap-filling by linear interpolation, allowing for maximum gap lengths of ≈ 2.5 km. These gap-filled periods are the ordinary BB_{bottom}. We declare precipitation below the presence of BB_{bottom} as rain and, if no bright band is found, as snowfall.

We account for a transition zone where mixed-phase precipitation is likely, as phase transitions do not occur immediately. We define periods of possible mixed-phase precipitation type by an additional interpolation over remaining data gaps of BB_{bottom} up to ≈ 2 km, and by extrapolation of BB_{bottom} of ≈ 2 km along the flight. Furthermore, mixed-phase precipitation becomes ubiquitous as the bright band descends to the surface. The near-surface BB reflectivities can then lead to an overestimation of precipitation rates. To prevent this, all corresponding precipitation periods with $BB_{\text{bottom}} < 300$ m are treated as uncertain.

The precipitation phase classification allows the derivation of precipitation rates to distinguish between snow and rain periods. This is essential as the Z-R and Z-S relationships are quite different due to different scattering properties of the hydrometeors. We consider six reflectivity-rate relationships (Table 1). Each of these relationships considers different aspects relevant for our Ka-band radar estimates of precipitation in Arctic ARs. In particular, the relationships weigh lower and higher reflectivity factor values differently. None of the relationships listed is optimal for our purposes. However, the variety of their different representativeness gives us a higher chance of reproducing the high PSD variability in AR conditions as found by Norris et al. (2020). Therefore, we apply all relationships to our precipitation-phase-classified reflectivities and consider their spread to estimate our uncertainties.

We find different precipitation modes for the first internal leg (Fig. 6). While the western post-frontal sector shows convective cells, there is very deep convection in the AR core and its eastern part belonging to S1, which contains two major precipitation fields (Fig. 6c). Further east in the pre-frontal sector (Fig. 6; right side), precipitation becomes weaker and more stratiform. While the cell in the post-frontal (cold) sector is snow, the melting layer in the heavy precipitation core rises towards the warm pre-frontal sector (Fig. 6b,c). Within the pre-frontal half of the core, precipitation contains rain with mean rates greater than $0.5\,\mathrm{mm\,h^{-1}}$, while the rates based on the relationship of Chandra et al. (2015) exceed $1\,\mathrm{mm\,h^{-1}}$. In particular, for more intense precipitation, the rates between the relationships increasingly diverge (Fig. 6c), leading to higher uncertainties in the precipitation estimate for the moisture budget closure. For the pre-frontal segment of the internal leg, we derive a mean precipitation rate of $0.05\,\mathrm{mm\,h^{-1}}$, with an uncertainty range from 0.01 to $0.11\,\mathrm{mm\,h^{-1}}$.

The Arctic precipitation rates are much lower than the airborne precipitation rates in mid-latitude ARs by Norris et al. (2020). Yet, our approach may underestimate precipitation because we neglect hydrometeor attenuation, which becomes relevant for estimates near the surface when the radar signal has to penetrate deep rain clouds. Obtaining estimates of the magnitude of melting layer attenuation is complex. The receivers' high pulse power and high sensitivity lead to overdriven ground return. This prevents approaches such as the path-integrated attenuation correction by Meneghini et al. (2015).

3.5 Moisture transport divergence (∇IVT) based on dropsondes

For the dropsonde-based determination of the IVT divergence, we follow the methods of Bony and Stevens (2019) and Dorff et al. (2024). We derive both composites of the moisture transport divergence, namely mass divergence (DIV_{mass}) and moisture advection (ADV_{q}) in Eq. 4, using a regression approach applied to the respective sonde-based wind and moisture fields. In case of linear variations, a time-stationary meteorological quantity Φ (e.g. wind speed) can be inferred as:

$$\Phi = \Phi_o + \frac{\delta\Phi}{\delta x}\cdot\Delta x + \frac{\delta\Phi}{\delta y}\cdot\Delta y, \tag{6}$$

where Φ_o is the area mean and Δx and Δy are zonal and meridional displacements from the area centre point. Using the values of Φ at sounding locations and minimising the least-squares errors in the linear regression fit of Eq. 6, linear estimates of the zonal (x) and meridional (y) gradients are obtained. We calculate the divergence by summing the two gradients. The uncertainty in derived divergence is estimated by Gaussian error propagation from the uncertainty of the fitted regression coefficients.
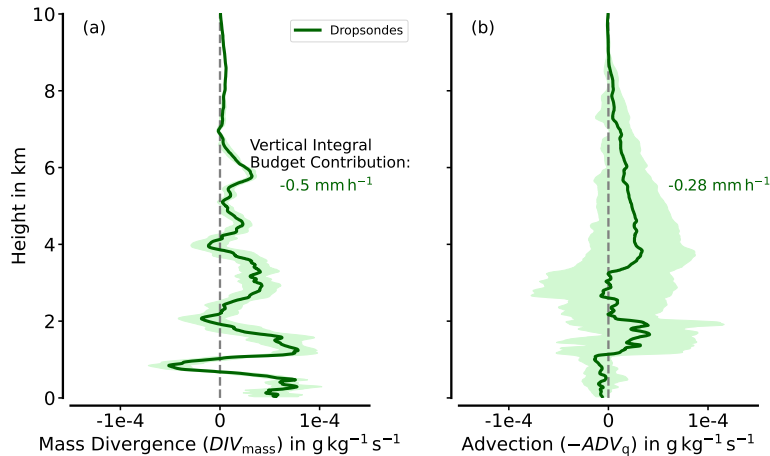
Figure 7. Sonde-based vertical profiles of mass divergence (a) and advection (b) for AR sector S1. Bold lines indicate the values based on the regression fits, while shaded areas mark the uncertainties resulting from the standard deviation in the regression fit components.

We determine both the divergence of the wind vector field and the gradients of the moisture field to calculate the two
370   components DIV_{mass} and ADV_{q} and finally as the sum of the vertical integral of both composites, $\nabla \cdot IVT$ (Eq. 4). Uncertainties of $\nabla \cdot IVT$ are non-trivial due to possible statistical dependence of values along the vertical profile. While Norris et al. (2020) used a Monte-Carlo approach to circumvent this limitation, we estimate the vertical decorrelation length by referring to a common low-level jet (LLJ) vertical extent of $400\,\mathrm{m}$. We average the uncertainties for DIV_{mass} and ADV_{q} in vertical $400\,\mathrm{m}$ bins, with the bin size as our decorrelation length estimate. We assume that these values are statistically independent, so we can
375   apply the Gaussian and central limit theorem. The uncertainty of the vertically integrated composites, $IDIV_{\mathrm{mass}}$ and $IADV_{\mathrm{q}}$ is calculated from the standard deviation of the respective uncertainty values in the $400\,\mathrm{m}$ bins, multiplied by the vertical pressure range and the number of pressure levels.

For S1, Fig. 7 shows the vertical profiles of DIV_{mass} and ADV_{q}, as derived from the sonde-based regression. For both composites, the values remain in the range of $\pm 1 \cdot 10^{-4}\,\mathrm{g\,kg^{-1}\,s^{-1}}$ and are rather low for Arctic AR conditions (Dorff et al.,
380   2024). Both composites contribute to the moisture budget through drying. Calculating the vertical integrals $IDIV_{\mathrm{mass}}$ and $IADV_{\mathrm{q}}$, mass divergence causes a drying of $0.50 \pm 0.06\,\mathrm{mm\,h^{-1}}$ and dry advection of $0.28 \pm 0.14\,\mathrm{mm\,h^{-1}}$, respectively.

Both composites act differently at vertical levels. Mass divergence is most pronounced in the lower levels up to $4\,\mathrm{km}$. Remarkably, the divergence is interrupted by a slight convergence at around $1\,\mathrm{km}$ (Fig. 7a). This is in the height of the LLJ (Ralph et al., 2005), where the sondes measure wind speeds above $30\,\mathrm{m\,s^{-1}}$. Mass convergence near the LLJ is typical for
385   ARs (Guan et al., 2020) and has also been identified in the Arctic ARs (Dorff et al., 2024). At this height, mass convergence is associated with supergeostrophic winds, which enhance the moisture transport (Demirdjian et al., 2020). Except for the LLJ, divergent winds dominate the mass divergence (Fig. 7a). While wind speeds remain similar along the mid-troposphere ($\approx 25\,\mathrm{m\,s^{-1}}$ up to $6\,\mathrm{km}$), horizontal wind divergence increases with height, mainly due to changes in wind direction. Still, the magnitude of moisture mass divergence (DIV_{mass}) decreases due to the superimposition of vertically decreasing moisture.
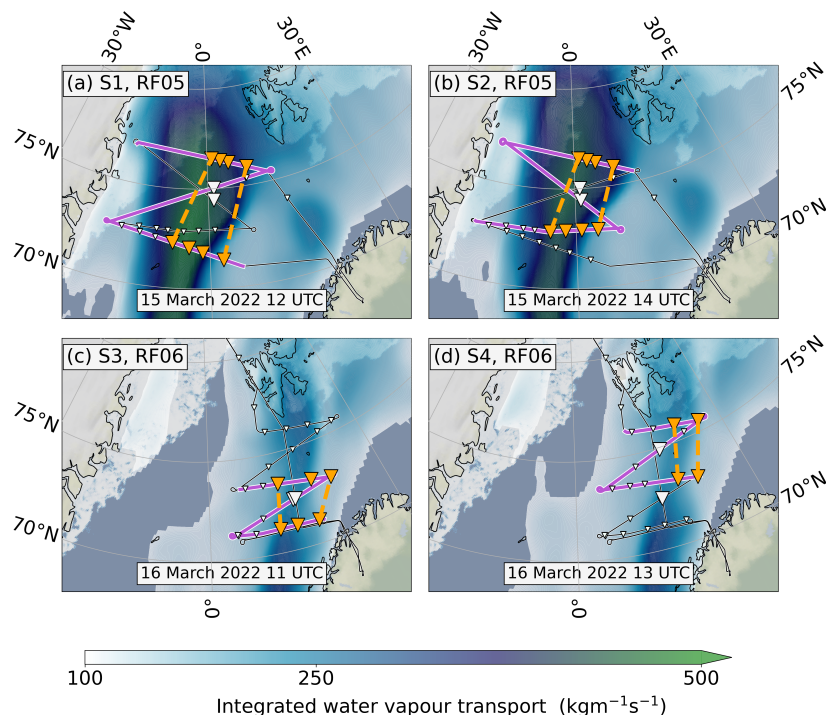
Figure 8. All four AR flight corridors sampled by the zigzag flight pattern (purple lines) in RF05 and RF06 (black/white lines). ERA5-IVT contours superimpose the sea ice map from AMSR2. Dropsondes are depicted by triangles, where orange triangles indicate the sondes spanning the pre-frontal sectors, S1-S4 (dashed orange lines). ERA5 time steps (bottom) refer to the centred hour of each zigzag pattern.

Moisture advection is low from the saturated boundary layer up to the LLJ (Fig. 7b). At these levels, all sondes indicate a very moist troposphere, with q around $4.5\,\mathrm{g\,kg^{-1}}$. While moisture in Arctic ARs can occasionally also exceed $5\,\mathrm{g\,kg^{-1}}$ in early summer (Viceto et al., 2022), such q values are exceptional for early spring conditions (Dorff et al., 2024). Above the LLJ, dry advection is relevant from 1-2 km and above 4 km. Since the horizontal moisture gradients persist with height more than mean absolute moisture, advection decreases less with height than mass divergence. The sondes in the inflow legs partly show very dry mid-level conditions (not shown). The uncertainties increase significantly and are much higher than for mass divergence.

4 Temporal evolution of airborne AR moisture budget components

4.1 Series of pre-frontal AR sectors

To assess the temporal evolution of the AR budget components (G2, Sect. 1), we analyse a series of four AR flight corridors encompassed by the two flights RF05 and RF06. Figure 8 illustrates how two zigzag patterns per RF sample the AR to derive its budget components over a period exceeding 24 h. During both RFs, the outflow leg of the first zigzag pattern simultaneously serves as the inflow leg in the zigzag pattern for the consecutive AR flight corridor. Aiming to derive the full moisture budget
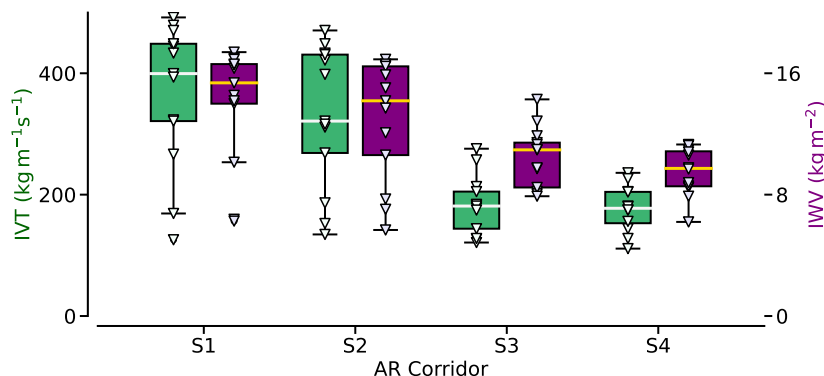
Figure 9. Box plots showing the statistics of sonde-based IVT (green) and IWV (purple) values within the four AR flight corridors, which are sampled from two consecutive days (S1, S2 belonging to research flight RF05, while S3, S4 to RF06). The boxes show the quartiles of the data sets. The statistics refer to all sondes released inside the zigzag flight corridor, not only the prefrontal sectors. Triangles depict the individual values of each sonde.

during the AR evolution from airborne observations, our analysis focuses on the pre-frontal AR sectors (Fig. 8; orange areas) due to the ATC restrictions on western sonde releases during RF05.

405   The relevant sondes in the zigzag patterns cover four pre-frontal sectors (S1-S4, Fig. 8). During RF05, the pre-frontal sectors S1 and S2 are located in the AR exit region, southwest of Svalbard, over the ice-free ocean, while in RF06, they are located south of Svalbard. The outflow leg of the last AR sector (S4) approaches the southern coast of Svalbard, crossing the marginal sea ice zone. The number of sondes used to calculate $\nabla \cdot IVT$ in each pre-frontal sector in S1 and S2 differs from S3 and S4 during RF06 (Fig. 8). Eight sondes per sector are included in the divergence calculations for S1 and S2 (RF05). In contrast, the pre-frontal flight legs in RF06 are shorter, resulting in only four to six sondes spanning the pre-frontal sectors. We account for

410   the impact of the number of sondes on the accuracy of $\nabla \cdot IVT$ by quantifying the uncertainty in the regression coefficients.

4.2   Decay of the atmospheric river

The reanalysis $\boldsymbol{IVT}$ fields in Fig. 8 reveal a significant decay of the AR. The extended AR core, which maintained $IVT \geq$ $400\,\mathrm{kg\,m^{-1}\,s^{-1}}$ during RF05 (Fig. 8a, b) substantially decreased to below $300\,\mathrm{kg\,m^{-1}\,s^{-1}}$ (Fig. 8c, d) by the next day. For the airborne perspective, Fig. 9 illustrates the sonde-based distributions of IWV and IVT derived along each flight corridor

415   corresponding to one of the AR pre-frontal sectors S1-S4 (Fig. 8). Comparing the sonde-based integrated quantities of the two flight days, the IVT values decrease by approximately $50\,\mathring{\%}$, while IWV decreases by $40\,\%$, indicating a stronger decay in the moisture transport than in the moisture fields. The box widths in Fig. 9 show that the spatial variability along the AR flight corridors decreases from those including S1 and S2 to those of S3 and S4. Similar to the median values, the decrease in variability is more pronounced for IVT than for IWV. Note that the sonde-based decay of IWV is similarly reproduced by

420   the continuous along-track representation of the HAMP-based IWV retrieval (not shown).

The distributions in Fig. 9 between two flight corridors on the same day are almost similar. Nonetheless, the medians still suggest a decaying trend of the AR on these shorter time scales. With this consistent decay of the AR, it is worth investigating how this trend can be linked to the evolution of the moisture budget components.

4.3 Comparing the moisture budget components

425 We compare all airborne moisture budget components, derived as described in Sect. 3, over the series of pre-frontal AR sectors, and determine to what extent each component contributes to the vertically integrated moisture budget (Eq. 1). For all budget components and pre-frontal sectors, Fig. 10 shows that the individual components contribute to the moisture budget in a range of $\pm 1\,\mathrm{mm\,h^{-1}}$. The magnitude of these ranges is slightly lower than the reanalysis-based statistics of mid-latitude AR events in Guan et al. (2020) and nearly half the size of the airborne components derived in the mid-latitude case study conducted by

430 Norris et al. (2020). However, our AR flight corridors and pre-frontal sectors are substantially larger than those in Norris et al. (2020). For Arctic conditions, the absolute magnitudes of $IDIV_\mathrm{mass}$ and $IADV_\mathrm{q}$, which we derive in our AR, are comparable to distributions found in pre-frontal AR sectors in Dorff et al. (2024).

Figure 10 shows that the AR experiences rather weak surface interaction, characterised by small mean contributions from evaporation (E) and precipitation (P). Specifically, evaporation remains notably weak, with the highest value of $E = 0.15\,\mathrm{mm\,h^{-1}}$

435 at the first sonde in Fig. 5 across both RFs. Moreover, the average pre-frontal precipitation based on the internal flight leg remains below $0.1\,\mathrm{mm\,h^{-1}}$. Despite cloud systems' compact and deep nature within the AR core, the surface precipitation is very heterogeneous. While precipitation rates up to $1\,\mathrm{mm\,h^{-1}}$ are derived for both rain and snow phases, they occur only for short periods. Rather, isolated moderate precipitation plumes often alternate with weak or no precipitation periods. Furthermore, stronger precipitation is partly found west of the pre-frontal budget regions.

440 The moisture transport divergence mainly controls the local change of water vapour for all sectors. Between advection and mass divergence, we identify mainly moisture (dry) advection aligned with the local water vapour change. This is consistent with mid-latitude ARs, where advection has been identified as being more correlated with local water vapour change (Guan et al., 2020). The mass convergence that governs the vertical motion that can trigger precipitation is very weak for this AR. According to Guan et al. (2020), the strong mass divergence during RF05 is atypical for pre-frontal AR characteristics.

445 The dominant components are those with the highest absolute uncertainties. Uncertainties in $\delta IWV/\delta t$ can reach up to $\pm$ $0.25\,\mathrm{mm\,h^{-1}}$ (e.g. S2; Fig. 10). A comparison of the two composites of $\nabla \cdot IVT$ shows that the uncertainties in advection are greater than those in mass divergence. This difference is due to higher spatial variability in the moisture field than in the wind field, which influences the uncertainty of the regression fits (Sect. 3.5) and thus affects the accuracy of the resulting budget components. Higher moisture variability has also been found in other Arctic ARs (Dorff et al., 2024). In addition, the

450 components show the dependence of the moisture transport representation on the sampling frequency (Ralph et al., 2017; Dorff et al., 2024). The sampling of S1 and S2 involved eight sondes along both cross-sections, while only six (four) were used for S3 (S4), as shown in Fig. 8. The sectors S3 and S4 exhibit much larger uncertainties in sonde-based integrated moisture transport divergence. Particularly, the uncertainties in S4 highlight that coverage by four sondes in a frontal sector may be insufficient.
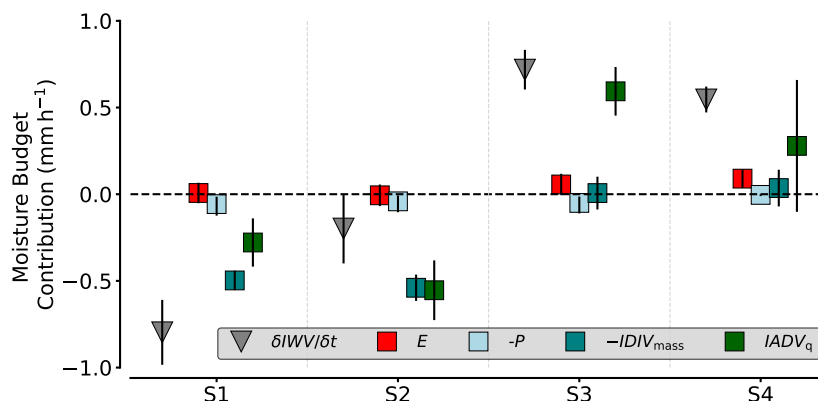
Figure 10. Hourly contribution in $\mathrm{mm\,h^{-1}}$ of the vertically-integrated moisture budget components (Eq. 1) for each of the pre-frontal sectors (S1-S4). Note that IVT convergence ($-\nabla \cdot IVT$) is split into both integrated summands, mass convergence (-$IDIV_{\mathrm{mass}}$) and moisture advection ($IADV_{\mathrm{q}}$). All components were derived from HALO. The error bars represent the uncertainties derived for each of the components.

During the decaying evolution, the magnitudes of the moisture budget components remain rather constant. However, the
455 values change in their sign. The pre-frontal AR sectors exhibit a drying of more than $0.5\,\mathrm{mm\,h^{-1}}$ during RF05 (S1 and S2),
in contrast to a surprising moistening of more than $0.5\,\mathrm{mm\,h^{-1}}$ during RF06. Throughout this transition, the balance of local
change in water vapour and moisture transport divergence, and the weak precipitation and evaporation, persists across all sec-
tors. The moisture transport divergence primarily contributes to the drying of the air masses during RF05 and the moistening
during RF06. Both composites of $\nabla \cdot IVT$ shift from divergence to convergence, while advection emerges as the predom-
460 inant component over the mass divergence. Since the trends in local moisture are mainly determined by moisture transport
divergence, we examine the vertical profiles of moisture advection ADV_{q} and mass divergence DIV_{mass} for all pre-frontal AR
sectors in more detail. This analysis enables a specification of the evolution of the moist air masses within the AR by identifying
the dominant heights of moisture transformation. We further examine how the cloud and precipitation fields respond.

4.4 Moisture transport divergence trends

465 Figure 11 offers insights into the evolution of moisture advection and mass divergence during the AR decay across the sectors
S1-S4, illustrating the dominant terms at different heights. During S1 and S2, almost the entire profile of DIV_{mass} exhibits
positive values, apart from the convergence peak at the LLJ at around $1.25\,\mathrm{km}$ (Fig. 11a). Compared to the first flight day
during S1 and S2 (Fig. 11a), S3 and S4 show lower amplitudes of DIV_{mass} along the vertical profile (Fig. 11c). DIV_{mass}
shifts towards more convergence, although with reduced amplitudes. The convergence peak at the LLJ widens, and another
470 convergence zone appears at about $2.5\,\mathrm{km}$. Although a broader low-level convergence zone arises, the sondes indicate that the
LLJ dissipates from RF05 towards RF06 (not shown). Wind speeds at the previous LLJ altitude decrease from $30\,\mathrm{m\,s^{-1}}$ in S1 to
less than $20\,\mathrm{m\,s^{-1}}$ in S4. This suggests that friction at the edges of the LLJ induces the entrainment of slower currents, widening
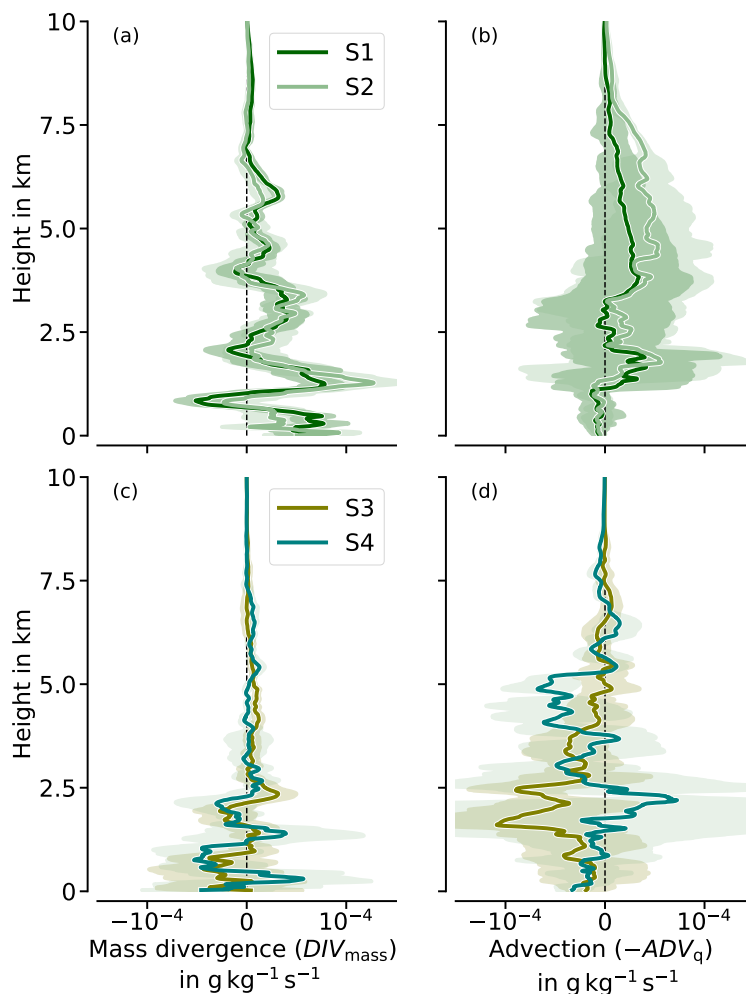
Figure 11. Vertical profiles of sonde-based moisture advection (negatively defined) and mass divergence for each of the pre-frontal AR corridors (S1-S4). The shadings indicate the uncertainties of the components based on the accuracy of the regression fits. For better visibility, values above 10 km are not considered due to their very minor contribution to $\nabla \cdot IVT$.

the LLJ but slowing its overall speed. From the lower mid-levels upwards, RF06 generally shows a significant decrease in mass divergence (Fig. 11a, c), so that mass divergence almost ceases to contribute to the moisture budget above 2.5 km.

475   For ADV_q, the dropsondes imply that the vertical characteristics undergo significant changes as well, though to a lesser extent within the marine boundary layer (<1 km). Despite the high moisture content, the marine boundary layer is well mixed, making advection a less dominant mechanism. During RF05 (Fig. 11b), dry advection prevails throughout the vertical profile on average, except for minor moisture advection around 2.5 km and in the marine boundary layer. Dry advection in mid-levels (3-7 km) intensifies notably from S1 to S2 but disappears during the second flight day (S3 and S4). In S3, moisture advection

480   peaks in lower levels ($-1 \cdot 10^{-4}\,\mathrm{g\,kg^{-1}\,s^{-1}}$ at about 2 km), while being negligible in the mid- and upper levels (Fig. 11b, d).

S4 shows significant moisture advection in the upper mid-levels ($-0.5{\cdot}10^{-4}\,\mathrm{g\,kg^{-1}\,s^{-1}}$ at 5 km), above dry advection around 2.5 km. However, all derived ADV_q values are subject to larger uncertainties than those of DIV_mass due to spatial moisture variability and they increase with larger sonde spacing during RF06. Particularly in S4 just below 2.5 km, the limited number of sondes (four) leads to an uncertainty range of approximately $\pm\,1.5{\cdot}10^{-4}\,\mathrm{g\,kg^{-1}\,s^{-1}}$ between dry and moisture advection. This variance contributes to the large uncertainty range in the integrated budget contribution of $IADV_\mathrm{q}$ (Fig. 10). Dropsondes from both flights indicate a very moist troposphere (not shown). Notably, the lower levels of the inflow cross-sections (up to 3 km) in S3 and S4 are much moister than S1 and S2. The highest q values are found in the marine boundary layer with $5\,\mathrm{g\,kg^{-1}}$ for RF06, attributed to moisture accumulation from intensified $\boldsymbol{IVT}$ in the AR remnants west of the Norwegian coast (Fig. 8d). The trends in moisture transport divergence raise the question of how the cloud and precipitation fields respond.

4.5 Trends in precipitation and cloud fields

Radar observations of the AR sectors indicate substantial changes in surface precipitation characteristics and cloud fields across the sectors (Fig. 12). Although precipitation overall contributes little to the moisture budget for all pre-frontal sectors in Fig. 10, it exhibits high spatial variability and differences between the sectors (Fig. 12). S1 shows moderate local precipitation rates of over $1\,\mathrm{mm\,h^{-1}}$, mostly falling as rain with a melting layer at about 1 km. While the second pre-frontal sector (S2) has much weaker precipitation, S3 exhibits higher rates, again with a more heterogeneous convective structure. Convection triggering is consistent with the sonde-based mass convergence in S3 (Fig. 11c). Despite similar low-level mass convergence in S4, substantial advection of dry and unsaturated air at 2 km height (Fig. 11d) here appears to hinder cloud formation and precipitation. The full internal legs reveal that precipitation in the post-frontal (cold) sector is mainly snow.

For S1 and S2, the AR embedded precipitating deep clouds reach up to 12 km. While the internal leg belonging to S1 shows two major cloud filaments (Fig. 12a), these filaments have merged during S2. The high cloud tops during RF05 persist in a subsiding and drying environment, presumably causing the clouds to dissolve slightly towards RF06. For the second day, the deeper clouds do not reach above 8 km. The lowering of the clouds coincides with the decreasing depth of vertical mixing (Fig. 11d) when the higher troposphere ($\geq 8\,\mathrm{km}$) exhibits a dynamical equilibrium. For S4, the cloud systems decouple from the boundary layer with a cloud base height between 2–4 km and a low cloud fraction underneath.

Summarising the trends of the budget components, we conclude that the IVT decay is not dominated by drying in lower levels but by a weakening of the winds. This weakening implies less spatial variability, resulting in lower mass divergence amplitudes and a reduced depth of vertical mixing and shallower cloud fields. The moisture transport divergence during RF05 is consistent with the directional dispersion of the $\boldsymbol{IVT}$ fields over the flight pattern (Fig. 8), leading to decreasing AR intensity and local drying. However, we neglected whether the components based on airborne observations robustly closed the moisture budget. If we aim to unravel air mass transformations within the AR by using the airborne budget components, we need to assess their plausibility by the magnitudes of emerging residuals in the budget closure of Eq. 1.
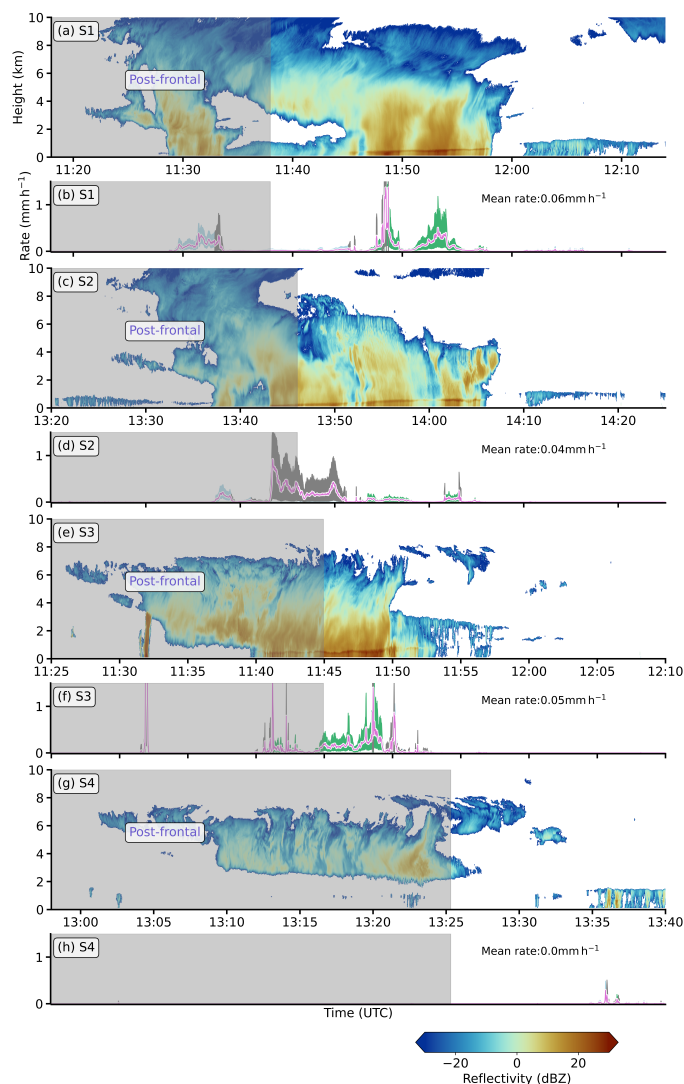
Figure 12. Radar-based cloud and precipitation fields of the four complete AR internal flight legs transecting the corresponding sectors S1-S4. Radar reflectivities (a, c, e, g) are shown with retrieved precipitation rates for snow (blue) and rain (green) resulting from our set of Z-R and Z-S relationships in (b, d, f, h), and its mean (pink). Uncertain phases (grey) consider both types of relationships. Coloured contours show the spread between the relationships. The left grey shaded areas correspond to the post-frontal western part of the internal legs.

5 Plausibility of airborne perspective on budget components

5.1 Residuals in budget closure

We calculate the residuals from the difference between retrieved $\delta IWV/\delta t$, based on HAMP measurements (Sect. 3.2), and
515 the sum of all other airborne components contributing to $\delta IWV/\delta t$ according to Eq. 1. Figure 13 shows that the mean residual
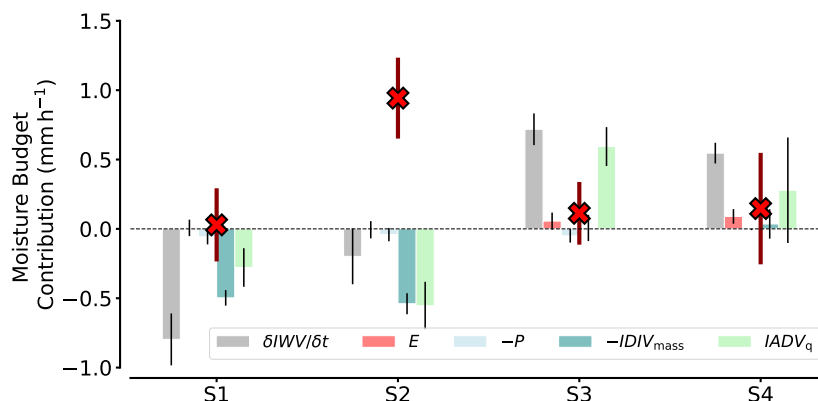
Figure 13. Residuals in airborne moisture budget closure for each pre-frontal AR sector (S1-S4). The residuals (red crosses) are shown with their uncertainties resulting from Gaussian error propagation of all budget component uncertainties. The bars repeat the values of all budget component contributions from Fig. 10 but are colour-coded paler.

for each sector is in the range of 0 to $1\,\mathrm{mm\,h^{-1}}$, indicating that the residuals are within the range of the main moisture budget components. Except for S2, the mean residual concerning HAMP-based $\delta IWV/\delta t$ results from a possible underestimation of sonde-based moisture transport divergence ($IADV_\mathrm{q} + IDIV_\mathrm{mass}$). S2 is notable for its high sonde-based moisture transport divergence, which, together with precipitation and condensation, overcompensates for the HAMP-based weak temporal water vapour change (drying). S2 is the only sector where the residual, together with its uncertainty range, is completely non-zero. For all other sectors, the moisture budget can be closed when the uncertainties of the budget components are included.

Further investigation on the origins and causes of the residuals will improve the interpretation of the plausibility of the airborne budget components. The following analysis of the residuals compares our airborne budget components with those from the ICON-2km and ERA5 model grid data (Sect. 2.2). The models serve as a valuable tool to examine factors influencing the airborne representation. By leveraging the models, we can test the sensitivity of the airborne budget components concerning sonde-based sampling frequency and the nonstationarity of the AR and we can investigate the airborne representativeness for the entire enclosed AR area. We use S1 as an example to assess the extent to which the airborne derivation and perspective of the budget components may differ from the actual prevailing components.

5.2 Sonde-based representativeness of IVT divergence

While sonde-based $\boldsymbol{IVT}$ provides high accuracy at individual points, the sporadic release of sondes leads to undersampling of moisture transport fields along the cross-sections, impacting the derivation of moisture transport divergence (Ralph et al., 2017; Dorff et al., 2024). We compare sonde-based moisture transport divergence (Fig. 14; green) with the model-based values from ICON-2km, collocated along the flight path and analysed at the sonde locations (Fig. 14; grey). For the along-track perspective, the model-observation comparison shows good agreement. The profiles generated by ICON at the sonde locations show similarity in moisture transport divergence (ADV_q and DIV_mass) with the actual sonde-based profiles. The vertical variability
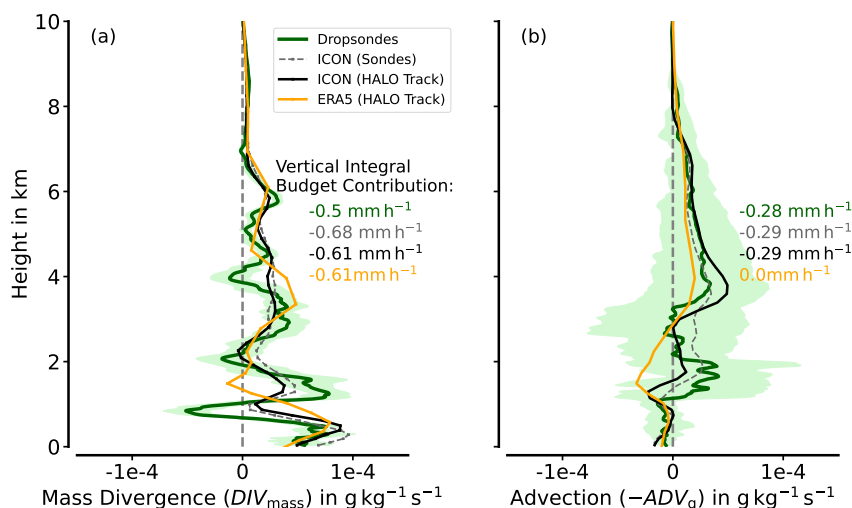
Figure 14. Along-track model-observation comparison of moisture transport divergence in S1. Sonde-based values are equivalent to those in Fig. 7. ICON values are interpolated onto the flight track and viewed in two resolutions. Once, ICON-based moisture transport divergence is derived from wind and moisture data only at the sonde locations, and the second is for continuous sampling along the AR cross-section legs. The latter represents the ideal sonde sampling for the given flight pattern. For an easy view, ERA5 is only shown in the continuous representation.

is higher in the sonde-based profiles. In particular, the significant mass convergence within the LLJ evident from the sondes is not adequately reflected by the ICON-2km mimicked sondes (Fig. 14a). Nonetheless, the ICON-2km mimicked sondes, and the real dropsondes show similar means of the integrated budget contributions, especially for $IADV_q$ (Fig. 14).

Compared to the continuous along-track representation in ICON-2km (Fig. 14; black-bold), undersampling from discrete soundings has little effect on the divergence values for both composites, namely ADV_q and DIV_{mass}. Differences in the moisture transport divergence between ICON values based on the sonde locations and those based on the continuous representation along the flight path are overall small, barely exceeding $0.1\,\mathrm{mm\,h^{-1}}$ (Fig. 14). The largest discrepancies occur in ICON-based dry advection (below 3 km), which is overestimated when considering only the sonde locations (Fig. 14b). The uncertainties at each height are slightly lower for the continuous ICON-2km (not shown). We find that the continuously collocated ERA5 (Fig. 14; orange) has difficulties in representing the low-level moisture transport divergence below 3 km, as there are large deviations from ICON-2km and dropsondes. This confirms ICON-2km as a robust model-based $\boldsymbol{IVT}$ divergence along the flight. The differences in ICON-based $\nabla \cdot IVT$ between the continuous and sporadic sonde releases sampling strategies are too small to attribute the undersampling of moisture transport by sondes as the main cause for the residuals reaching up to $1\,\mathrm{mm\,h^{-1}}$.

As a second effect, Dorff et al. (2024) emphasize the temporal evolution of the AR, causing nonstationarity that represents a relevant source of error for sonde-based estimates of moisture transport divergence. In our case, both models reproduce stronger advection of moisutre in the instantaneous view compared to the non-instantaneous observations (not shown). This stronger advection would, in turn, increase the residuals.
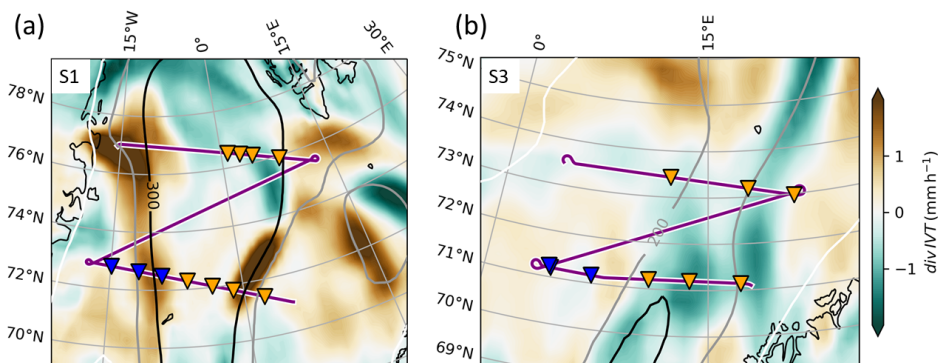
Figure 15. ERA5-based $\nabla \cdot IVT$ (colour-coded) for the centred hours of the zigzag patterns for S1 (a) and S3 (b). Flight tracks spanning the sectors and sondes (triangles) are superimposed (pre-frontal in orange, post-frontal in blue). Greyish contour lines show $\boldsymbol{IVT}$ in $\mathrm{kg\,m^{-1}\,s^{-1}}$.

Nonstationarity becomes most effective in deviating the airborne results when there is a high subscale spatial variability. Not only did the zigzag pattern take quite a long time, especially in RF05, but it also aimed to represent the divergence in a very large

555   AR flight corridor. To further investigate the subscale spatial variability within the AR flight corridor, we examine the ERA5 moisture transport divergence field product. Figure 15a illustrates a pronounced dipole structure in the ERA5-based $\nabla \cdot IVT$ field within the pre-frontal sector of the AR flight corridor. While the southern region and the inflow leg exhibit divergence with budget contributions of $\nabla \cdot IVT \le -1\,\mathrm{mm\,h^{-1}}$, the northern region is characterised by convergence and positive moisture rates of about $1\,\mathrm{mm\,h^{-1}}$. This dipole is averaged out when the divergence calculations are based solely on the two cross-sections,

560   resulting in lower airborne estimated budget contributions. An important factor for the divergence pattern in Fig. 15a is the expansion of the $\boldsymbol{IVT}$ field north of the inflow cross-section induced by changes of the transport (wind) direction (see Fig. 2a). This change in wind direction within the flight corridor is reflected in the sonde-based predominance of DIV_{mass} against ADV_{q}. Furthermore, the dipole structure can clarify the along-track discrepancies between ICON-2km and ERA5. While the models are confident about $\boldsymbol{IVT}$ spreading north of the internal leg, slight variations in the dipole pattern result in differing

565   characteristics from the airborne perspective on $\nabla \cdot IVT$. Thus, although the divergence calculations based on sonde data and the models align reasonably well along the flight path, their representativeness for the entire budget region is limited. In RF06, such dipole structures are absent (Fig. 15b). Instead, a more distinct zone of overall $\boldsymbol{IVT}$ convergence is identified. This indicates that the sampling in the AR flight corridors during RF06 is more representative despite fewer sondes.

5.3   Representativeness of airborne precipitation rates

570   The high precipitation rates due to this AR observed at Svalbard, with more than $30\,\mathrm{mm}$ per day as reported by Walbröl et al. (2024), seem to contrast with the relatively low precipitation estimates along the AR flight corridor. However, the radar demonstrates the heterogeneity of precipitation within the AR, with local regions experiencing moderate precipitation (Fig. 6). This raises concerns regarding the representativeness of the airborne radar-derived estimates. In particular, the curtain-based
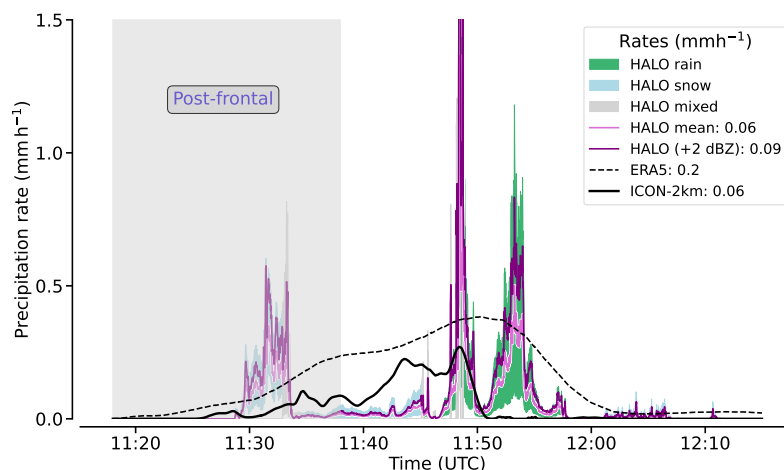
Figure 16. Precipitation rates along the internal flight leg of S1 (RF05). Shaded areas represent the uncertainty ranges arising from the minimum and maximum relationship values. Violet lines give mean radar precipitation. The darker line depicts precipitation rates based on simplified attenuation imitation (+2 dBZ). ICON and ERA5-based curves represent model precipitation along the flight. Legend values yield the respective means of pre-frontal precipitation. The post-frontal part of the internal leg is presented but neglected in the mean.

perspective of the radar may not capture the considerable variability in cloud conditions (Dorff et al., 2022). Additionally, the
575   missing correction for hydrometeor radar attenuation is a limitation of the airborne estimates.

     Therefore, we revisit the comparison of the airborne data with the model data, focusing initially on precipitation from the along-track perspective. We compare the radar observations with the collocated ICON-2km and ERA5. Figure 16 shows the radar and the model data precipitation rates along the first internal leg belonging to S1. For the pre-frontal part of the internal leg, the mean precipitation in the along-track ICON-2km closely aligns with the radar-based precipitation estimates. At the
580   same time, ERA5 shows significantly higher values in a few regions. ICON-2km shows greater fluctuations than ERA5 due to its finer horizontal resolution (Sect. 2.2), but it is much more homogeneous with lower spatial variability than the radar data. While ERA5 estimates a mean precipitation of $0.2\,\mathrm{mm\,h^{-1}}$, its amplitude remains below $0.5\,\mathrm{mm\,h^{-1}}$ and is even lower in ICON-2km. The two pre-frontal precipitation maxima seen in the radar data, with local rates exceeding $1\,\mathrm{mm\,h^{-1}}$, are also found in ICON-2km, albeit with slight spatial shifts and smoothened with smaller local maxima.

585   The low radar-based precipitation mean could suggest an airborne underestimation, especially as the radar is uncorrected for hydrometeor attenuation. Specifically, the attenuation at the melting layer due to riming is mostly relevant. Li and Moisseev (2019) provide regression-based coefficients to quantify the attenuation by the melting layer and rain based on predetermined rain rates and reflectivities. We apply these coefficients to the rain rates in Fig. 16 and deduce a radar attenuation of up to 2 dBZ. To have a conservative estimate of the maximum underestimation of precipitation caused by attenuation, we thus increase all
590   reflectivities by 2 dBZ. These elevated radar reflectivities increase the mean precipitation rate by $0.03\,\mathrm{mm\,h^{-1}}$ (50 %) in Fig. 16. Radar-based precipitation estimates become more intense than that from ICON-2km, but ERA5 still indicates significantly stronger precipitation. However, ERA5 is known to overestimate Arctic precipitation (Wang et al., 2019; Schyberg et al., 2021).
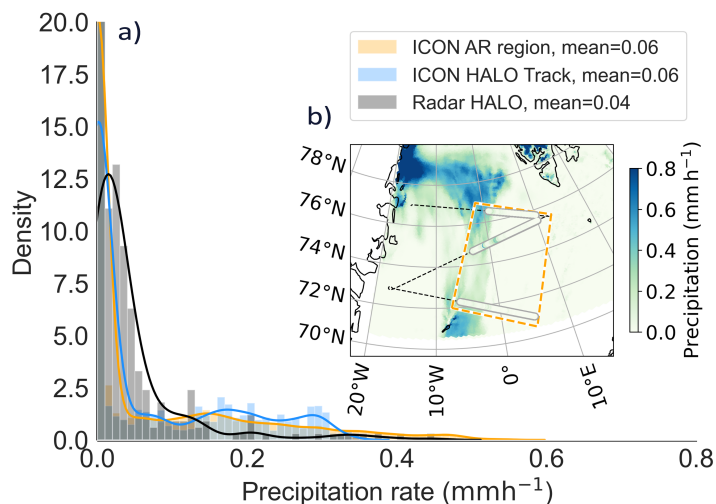
Figure 17. Kernel density estimate (KDE) of precipitation in the AR flight corridor of S1. Statistics refer to both the along-track precipitation rates and the rates for the entire AR flight corridor. (b) illustrates the spatial variability of ICON-based surface precipitation in the AR corridor S1 (orange-dashed) for the ICON output at the centred flight hour and highlights radar-based values along the flight. Here, in- and outflow leg parts of the pre-frontal sector are included.

Irrespective of attenuation effects, the high spatial variability of precipitation from the radar, and to some extent from ICON-2km, underscores the complexity of accurately representing precipitation conditions in an entire budget flight corridor using data from a single along-track curtain. Therefore, we compare the along-track distribution of precipitation rates with the horizontal distribution across the AR using the 2D surface field data from ICON-2km (Fig. 17). We average the radar reflectivities every 10 s to improve the comparability of the radar and ICON-2km data by achieving a similar horizontal resolution ($\approx 2.5\,\mathrm{km}$). Along the flight track, ICON reveals dominance of moderate precipitation rates ranging from 0.15–$0.35\,\mathrm{mm\,h^{-1}}$, while the radar shows higher rates, but these are hardly relevant for the kernel density estimate (KDE) in Fig. 17a.

When incorporating the horizontal ICON precipitation field, both the KDE and the spatial precipitation pattern (Fig. 17a, b) show that the flight path misses several precipitation regions within the AR corridor. The northern area of the AR flight corridor has stronger precipitation that is underrepresented by the airborne radar. Over the flight corridor area, the precipitation rate KDE (Fig. 17a; orange) resembles more a Weibull distribution, but higher precipitation rates contribute more than in the radar (Fig. 17a). Note that the spatial shift of the precipitation rates along the track in Fig. 17b is attributed to the temporal variations in AR dynamics during the zigzag manoeuvre, contrasting with the instantaneous model depiction.

Concluding the plausibility analysis of Sect. 5, we find a considerable subscale variability in the budget components within the AR flight corridors. Combined with the curtain-based sampling, this variability largely accounts for the residuals in the airborne budget closure. Our airborne analysis reveals the significance of small-scale precipitation within Arctic ARs as a key finding. Future research efforts can expand upon the comparison between model-derived and observed precipitation using the remaining AR flight segments of HALO-$(\mathcal{AC})^3$ (Walbröl et al., 2024; Wendisch et al., 2024).

6 Conclusions

This study pioneered the derivation of the atmospheric moisture budget components in an Arctic atmospheric river (AR) using airborne measurements. The intense Arctic AR traversed the Greenland Sea and the Norwegian Sea toward the Arctic sea ice. Four zigzag patterns (S1-S4) flown by the High Altitude and LOng Range Research Aircraft (HALO) examine the moisture

615 budget components during the dissipation phase of the AR in pre-frontal sectors. The airborne components were compared with model results to elucidate difficulties in the representativeness of the airborne components. We synopsise our achieved research goals as follows:

- **To derive all moisture budget components in Arctic ARs from a research aircraft (G1):** Our methods confirm the feasibility of deriving the moisture budget components using measurements from instruments on a single aircraft.

620 Dropsonde data enable the calculation of IVT divergence by measuring moisture and wind profiles at the inflow and outflow cross-sections, with near-surface dropsonde data used for estimating evaporation. Using training datasets from ERA5, a regression retrieval diagnoses IWV from brightness temperatures (T_B) measured by 25 microwave channels of an airborne radiometer, showing good agreement with dropsonde data (RMSE < $0.5\,\mathrm{kg\,m^{-2}}$). The regression retrieval is computationally efficient and adaptable for different training data of different regions. However, the regression retrieval

625 is unsuitable for sea ice-covered regions due to sea ice emissivity variations (Zabolotskikh and Azarov, 2022) and non-linear masking effects on microwave brightness temperatures. We derive precipitation rates from nadir Ka-band radar reflectivities, correcting for gaseous attenuation following Rosenkranz (1998). To account for uncertainties, we consider a set of Z-R/ Z-S relationships. Rain and snow are coexistent in the AR despite the high latitude and season. Omnipresent melting layers require estimations of attenuation to correct the precipitation rates. Therefore, we make a conservative

630 estimate of a maximum attenuation of 2 dBZ based on Li and Moisseev (2019). While all airborne-based moisture budget components involve significant uncertainties, these remain smaller than the actual component magnitudes.

- **To examine how the moisture budget components evolve during the dissipation phase of the AR (G2):** The temporal evolution of IVT indicates the dissipation of the AR due to reducing moisture transport. Despite the IVT decay, the absolute magnitude of the moisture budget components remains rather constant in the pre-frontal sectors. The compo-

635 nents contribute to the moisture budget in a range of $\pm 1\,\mathrm{mm\,h^{-1}}$, slightly lower than what is found in mid-latitude ARs (Guan et al., 2020). Within the Arctic AR, the moist air masses show little interaction with the surface regarding precipitation and evaporation. Local changes in IWV are primarily driven by moisture transport divergence via advection. This connection aligns with studies on pre-frontal moisture budget components in mid-latitude ARs (Cobb et al., 2021a; Guan et al., 2020) and with the role of moisture transport in shaping regional Arctic moisture patterns (Nygård et al.,

640 2020). However, the drying in the pre-frontal sector partly contrasts with patterns seen in mid-latitudes, where this sector is typically associated with moisture advection. The pre-frontal sectors indicate a change from a local drying towards a moistening on the second day. The spreading of the IVT field on the first day is driven by the pressure field causing directional divergence, which results in mass-divergent drying of $-0.53 \pm 0.07\mathrm{mm\,h^{-1}}$ (S2), but the heterogenous precipitation and deep clouds resist the moisture transport divergence. On the second day, the convergence of moisture

transport, which is dominated by moisture advection ($0.59 \pm 0.14 \, \mathrm{mm \, h^{-1}}$, S3), causes the moistening of the atmosphere. Throughout both flight days, the sondes indicate that the marine boundary layer maintains moisture with $q > 4 \, \mathrm{g \, kg^{-1}}$, while advection contributes more in mid-levels. The winds decrease significantly, with a dissipation of the LLJ.

- **To assess how accurate and representative the airborne budget components are for the entire AR flight corridor (G3):** The budget closure using the mean airborne budget components results in significant residuals for all sectors, with magnitudes of 0-1 $\mathrm{mm \, h^{-1}}$, comparable to dominant budget components. With the component uncertainties included, the moisture budget can be closed for all sectors except S2. Compared to the mimicked budget components along the flight using ICON-2km and ERA5, the airborne values are realistic and consistently indicate either drying or moistening. We find a sensitivity of $\nabla \cdot IVT$ values to the sonde spacing, but sonde-based $\nabla \cdot IVT$ differs by less than 25 % from that of mimicked continuous sampling. The observed precipitation rates are in better agreement with ICON-2km than with ERA5. The airborne observations provide a high spatial resolution of along-track precipitation and the vertical variability of the moisture transport divergence, although their spatial representativeness across the entire sector is limited. ICON-2km indicates that most precipitation fields are north of the internal leg. Additionally, even with an idealised continuous $\boldsymbol{IVT}$ sounding along the flight track, the spatial subscale variability between the two cross-section legs remains predominant. In the largest AR flight corridors (S1, S2), a horizontal dipole structure in $\nabla \cdot IVT$ is unresolved by the flight curtain. This subscale variability underscores the limitations of the flight pattern when the meridional distance between the cross-section legs is too large, which hampers an airborne budget closure.

Our closure of the moisture budget using the airborne platform HALO builds upon recent studies on airborne moisture budget components in ARs (e.g. Neiman et al., 2014; Norris et al., 2020). An innovative aspect of our study is that we do not require additional observation platforms. Notwithstanding, we recommend further comparisons with spaceborne spatial IWV fields in follow-up studies to assess the capabilities of both measurement platforms. Like Norris et al. (2020), we highlight the necessity of quantifying uncertainties for an observational moisture budget closure. While different techniques to derive the airborne budget components are worth investigating for this AR, the good agreement between our airborne budget components and the airborne-mimicked model representation underscores the reliability of our observational estimates.

The airborne results during RF05 are hampered by their reduced spatial representativeness, with significant subscale spatial variability not captured by the flight curtain. Future flight patterns should maintain the long cross-sections across the AR while reducing the distance between them. Shortening the meridional extent and, thus, the flight duration may lessen the impact of nonstationarity, resulting in improved divergence estimates. Dorff et al. (2024) indicate that flight duration is more relevant than sonde spacing for the misrepresentation of $\nabla \cdot IVT$. Nevertheless, the uncertainty ranges of the residuals confirm the feasibility of the airborne moisture budget closure, which is of great benefit for upcoming AR studies. The feasibility concretises future airborne research with regard to Arctic AR moisture budget components.

HALO-$(\mathcal{AC})^3$ offers a wealth of data in the Arctic ARs with a particular focus on the evolution and transformation of air masses during the ocean-sea ice transition, which is a highly relevant area of interest. While our study tracks an AR over two days to compare the evolution of the budget components as the AR dissipates, we lack quasi-Lagrangian matches of air

masses. Trajectory analyses indicate more revisits of matching air masses for different AR events during HALO-$(\mathcal{AC})^3$ (Ehrlich
et al., 2024). However, these observations exhibit complexity for the derivation of the budget components due to fewer sonde
releases and the difficulty of retrieving IWV over sea ice. Such a retrieval would facilitate comparisons of budget components
across changing surface types to explore whether AR air masses ascend over sea ice, potentially impacting the near-surface
inversion as suggested by e.g. You et al. (2022), and to examine the responses of moisture and clouds. HALO-$(\mathcal{AC})^3$ provides
many observations for the characterisation of AR precipitation (e.g. Walbröl et al., 2024; Wendisch et al., 2024), which has
been studied from reanalyses in Lauer et al. (2023). In particular, the novel high-resolution C3S Arctic Regional Reanalysis
(CARRA, Schyberg et al., 2021) could be evaluated with the radar data. The airborne investigation of Arctic ARs is far from
exhausted. The model-observation comparison by such long-range research aircraft reveals both the limitations and strengths
of each perspective. The combination of the perspectives delivers further clarity in the role of Arctic moist air intrusions, which
are dominated by ARs and are expected to increase in frequency and intensity in future climate (Kolbe et al., 2023).

Appendix A: Retrieval specifications

A1   Retrieval architecture and training data

The IWV is retrieved from the brightness temperatures (T_B) measured by the radiometer channels of the HALO Microwave
Package (HAMP) using a quadratic regression retrieval. For the frequency channels i, the regression relates measured $T_{\mathrm{B}i}$ to
IWV by:

$$IWV = \sum_i a_i \cdot T_{\mathrm{B},i}^2 + b_i \cdot T_{\mathrm{B},i} + c \tag{A1}$$

with the regression coefficients a_i, b_i, and the offset c. The Passive and Active Microwave TRAnsfer tool (PAMTRA; Mech
et al., 2020) is used to create a synthetic training data set to derive the regression coefficients for all HAMP channels at
flight altitudes from 7 to 16 km with 200 m intervals. ERA5 fields of moisture, temperature, wind, hydrometeors, and surface
properties for a domain over the North-Atlantic (65 to 89°N, -30 to 50°E) and 100 random days from 1979 to 2020, are used as
atmospheric input for PAMTRA. Nine AR events from Dorff et al. (2024) containing IWV values up to 20 kg m^{-2} were added
to tune the training data for AR conditions. The entire training data focuses on atmospheric profiles over the open ocean only,
as the sea ice emissivity in the microwave spectrum is often unknown and very complex, making the retrieval of atmospheric
properties over ice from microwave observations difficult. We conduct a least-squares fitting to the quadratic terms of the
synthetic T_Bs and ERA5-IWV to obtain the retrieval coefficients in Eq. A1.

A2   Retrieval performance

For the training data of ERA5-IWV and synthetic HAMP-T_Bs, the correlation coefficients range from 0.59 to 0.92 for the
K-band channels, three V-band channels (51.76, 52.8, 53.75 GHz), and the F-band channels near the 118.75 GHz oxygen ab-
sorption line. Conversely, the G-band channels around 183 GHz exhibit a partially negative correlation because the warmer
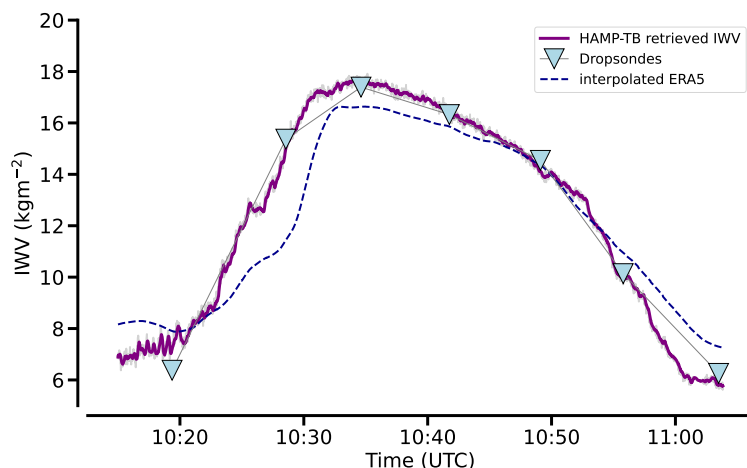
Figure A1. IWV along the first AR cross-section from RF05. Dropsonde-based IWV (triangles) are compared with the HAMP-based retrieved IWV (grey) that is smoothed using a 10 s running mean (purple). Aircraft collocated continuous ERA5-IWV is shown in blue.

lower troposphere is concealed by mid- and upper tropospheric water vapour and due to cloud ice sensitivity. Thus, unlike the

710 retrieval in Jacob et al. (2019), our retrieval incorporates all HAMP channels. This incorporation enables us to consider additional dependencies from the F-band channels and to address masking effects caused by hydrometeors at higher frequencies. To account for natural noise, all synthetic T_Bs have a noise with a normal distribution and a standard deviation of 0.5 K for the K- and V-band, and 1 K for the F-, W- and G-band, following Mech et al. (2014). We conduct the least-squares fitting to the synthetic T_Bs and ERA5-IWV to obtain the retrieval coefficients of Eq. 6 which we apply to the HAMP-T_B measurements.

715 To improve the comparability to dropsonde data, a 10 s running mean is applied to the HAMP retrieval output due to the noisy IWV retrieval values (Fig. A1). The retrieved IWV shows reasonable agreement with the dropsonde-based IWV over a wide range from 6–18 kg m^{-2} (Fig. A1). Both airborne datasets show the bell-shaped curve of IWV commonly seen in AR cross-sections (Ralph et al., 2017). We derive a root-mean-square error (RMSE) of 0.42 kg m^{-2} between retrieved IWV and sonde-based IWV, with the largest deviations at the highest IWV. For the sondes, George et al. (2021) report on a dry-bias,

720 but for HALO-$(\mathcal{AC})^3$ a correction was not necessary as the sondes were reconditioned before flight (Ehrlich et al., 2024).

The comparison of the airborne retrieved IWV values with the collocated and continuous ERA5-based representation (Sect. 2.2) confirms that the continuous HAMP representation reasonably replicates the IWV values. In particular, the cross-sectional IWV shape is very similar in ERA5 to the HAMP retrieved IWV, with a steeper pre-frontal IWV increase against the postfrontal decline. In turn, the IWV amplitudes in ERA5 are lower and only reach up to 16 kg m^{-2} (Fig. A1). Since ERA5 also

725 shows lower values than the dropsondes, we conclude an underestimation of IWV in the reanalysis, where the sondes of these flights were not assimilated (Ehrlich et al., 2024). A slight shift is observed in the ERA5-based IWV representation, where the rapid increase in IWV occurs further east (3 min later than observed). However, we do not attribute this shift solely to a misrepresentation by the reanalysis but rather to the spatio-temporal interpolation between the hourly outputs of ERA5.

Code and data availability. The code by HD that derives the airborne moisture budget components and conducts the presented analyses

730 with the illustrated figures can be accessed under Dorff (2024). The airborne data of the unified HAMP measurements is published under PANGAEA (Dorff et al., 2023), as well as the processed dropsonde Level-2 data (George et al., 2024), and are further described in Ehrlich et al. (2024). ERA5 data (Hersbach et al., 2018) were accessed from the Copernicus Climate Change Service (C3S) Climate Data Store (CDS). The ICON-2km simulations can be provided upon request.

Author contributions. HD, FA and HK were the main initiators for the work in the scope of this manuscript. FA and HK helped conceptualize

735 the manuscript and the flight pattern for the airborne moisture budget closure. VS and FE planned the flights for the analyzed cases as mission PIs under the support of DO, AW, MW and HD. HD derived all airborne moisture budget components, while FE calibrated the radar data and provided attenuation estimates, AW supported the radiometer processing and VS and DO were responsible for running the ICON simulations. MM helped to develop the IWV retrieval by configuring PAMTRA for this study. HD conducted the budget analysis presented, created the figures, and drafted the manuscript under the scientific supervision of FA and HK. All authors contributed to revising the manuscript.

740 *Competing interests.* The authors declare that they have no conflict of interest.

Acknowledgements. We are grateful for the funding of project grant no. 316646266 by the Deutsche Forschungsgemeinschaft (DFG, German Research Foundation) within the Priority Programme SPP 1294 framework to promote research with HALO. This work also used the resources of the Deutsches Klimarechenzentrum (DKRZ) granted by its Scientific Steering Committee (WLA) under project ID bb1086. Furthermore, we explicitly acknowledge the German Airspace Center for providing the HALO research aircraft for this research. We ap-

745 preciate the funding and support from TRR 172 by the Deutsche Forschungsgemeinschaft (DFG, German Research Foundation, Project-ID 268020496), within the Transregional Collaborative Research Center's Arctic Amplification: Climate Relevant Atmospheric and Surface Processes, and Feedback Mechanisms $(\mathcal{AC})^3$ to make HALO-$(\mathcal{AC})^3$, such a huge campaign, possible. We thank the entire scientific team of HALO-$(\mathcal{AC})^3$ and the aircraft crew for realizing this campaign and the AR research flights. All of them are listed as authors in Wendisch et al. (2024). Thanks also go to Norbert Noreiks for delivering sketches of the research aircraft.

References

750 ASPEN: Aspen | Earth Observing Laboratory (last accessed: 2024-10-24), https://www.eol.ucar.edu/sofware/aspen, 2024.

Austen, D.: Precipitation rates in Arctic moist air intrusions from airborne radar measurements [B.Sc. Thesis], 2022.

Barrett, A. P., Stroeve, J. C., and Serreze, M. C.: Arctic Ocean Precipitation From Atmospheric Reanalyses and Comparisons With North Pole Drifting Station Records, Journal of Geophysical Research: Oceans, 125, https://doi.org/10.1029/2019jc015415, 2020.

755 Bintanja, R., van der Wiel, K., van der Linden, E. C., Reusen, J., Bogerd, L., Krikken, F., and Selten, F. M.: Strong future increases in Arctic precipitation variability linked to poleward moisture transport, Science Advances, 6, https://doi.org/10.1126/sciadv.aax6869, 2020.

Bony, S. and Stevens, B.: Measuring Area-Averaged Vertical Motions with Dropsondes, Journal of the Atmospheric Sciences, 76, 767–783, https://doi.org/10.1175/jas-d-18-0141.1, 2019.

Bresson, H., Rinke, A., Mech, M., Reinert, D., Schemann, V., Ebell, K., Maturilli, M., Viceto, C., Gorodetskaya, I., and Crewell, S.: Case
760 study of a moisture intrusion over the Arctic with the ICOsahedral Non-hydrostatic (ICON) model: resolution dependence of its representation, Atmospheric Chemistry and Physics, 22, 173–196, https://doi.org/10.5194/acp-22-173-2022, 2022.

Chandra, A., Zhang, C., Kollias, P., Matrosov, S., and Szyrmer, W.: Automated rain rate estimates using the Ka-band ARM zenith radar (KAZR), Atmospheric Measurement Techniques, 8, 3685–3699, https://doi.org/10.5194/amt-8-3685-2015, 2015.

Cobb, A., Michaelis, A., Iacobellis, S., Ralph, F. M., and Monache, L. D.: Atmospheric River Sectors: Definition and Characteristics Ob-
765 served Using Dropsondes from 2014–20 CalWater and AR Recon, Monthly Weather Review, 149, 623–644, https://doi.org/10.1175/mwr-d-20-0177.1, 2021a.

Cobb, A., Monache, L. D., Cannon, F., and Ralph, F. M.: Representation of Dropsonde-Observed Atmospheric River Conditions in Reanalyses, Geophysical Research Letters, 48, https://doi.org/10.1029/2021gl093357, 2021b.

Crewell, S., Ebell, K., Konjari, P., Mech, M., Nomokonova, T., Radovan, A., Strack, D., Triana-Gómez, A. M., Noël, S., Scarlat, R.,
770 Spreen, G., Maturilli, M., Rinke, A., Gorodetskaya, I., Viceto, C., August, T., and Schröder, M.: A systematic assessment of water vapor products in the Arctic: from instantaneous measurements to monthly means, Atmospheric Measurement Techniques, 14, 4829–4856, https://doi.org/10.5194/amt-14-4829-2021, 2021.

Dacre, H. F., Martínez-Alvarado, O., and Mbengue, C. O.: Linking Atmospheric Rivers and Warm Conveyor Belt Airflows, Journal of Hydrometeorology, 20, 1183–1196, https://doi.org/10.1175/jhm-d-18-0175.1, 2019.

775 Demirdjian, R., Norris, J. R., Martin, A., and Ralph, F. M.: Dropsonde Observations of the Ageostrophy within the Pre-Cold-Frontal Low-Level Jet Associated with Atmospheric Rivers, Monthly Weather Review, 148, https://doi.org/10.1175/mwr-d-19-0248.1, 2020.

Dipankar, A., Stevens, B., Heinze, R., Moseley, C., Zängl, G., Giorgetta, M., and Brdar, S.: Large eddy simulation using the general circulation model ICON, Journal of Advances in Modeling Earth Systems, 7, 963–986, https://doi.org/10.1002/2015ms000431, 2015.

Dorff, H.: Scientific Code for Moisture Budget Closure Analysis in Atmospheric River from HALO-(AC)[3] [code],
780 https://doi.org/10.5281/ZENODO.13152516, 2024.

Dorff, H., Konow, H., and Ament, F.: Horizontal geometry of trade wind cumuli – aircraft observations from a shortwave infrared imager versus a radar profiler, Atmospheric Measurement Techniques, 15, 3641–3661, https://doi.org/10.5194/amt-15-3641-2022, 2022.

Dorff, H., Aubry, C., Ewald, F., Hirsch, L., Jansen, F., Konow, H., Mech, M., Ori, D., Ringel, M., Walbröl, A., Crewell, S., Ehrlich, A., Wendisch, M., and Ament, F.: Unified Airborne Active and Passive Microwave Measurements over Arctic Sea Ice and Ocean during the
785 HALO-(AC)[3] Campaign in Spring 2022 [data set], https://doi.org/10.1594/PANGAEA.963250, 2023.

Dorff, H., Konow, H., Schemann, V., and Ament, F.: Observability of moisture transport divergence in Arctic atmospheric rivers by dropsondes, Atmospheric Chemistry and Physics, 24, 8771–8795, https://doi.org/10.5194/acp-24-8771-2024, 2024.

Dufour, A., Zolina, O., and Gulev, S. K.: Atmospheric Moisture Transport to the Arctic: Assessment of Reanalyses and Analysis of Transport Components, Journal of Climate, 29, 5061–5081, https://doi.org/10.1175/jcli-d-15-0559.1, 2016.

790 Ehrlich, A., Crewell, S., Herber, A., Klingebiel, M., Lüpkes, C., Mech, M., Becker, S., Borrmann, S., Bozem, H., Buschmann, M., Clemen, H.-C., De La Torre Castro, E., Dorff, H., Dupuy, R., Eppers, O., Ewald, F., George, G., Giez, A., Grawe, S., Gourbeyre, C., Hartmann, J., Jäkel, E., Joppe, P., Jourdan, O., Jurányi, Z., Kirbus, B., Lucke, J., Luebke, A. E., Maahn, M., Maherndl, N., Mallaun, C., Mayer, J., Mertes, S., Mioche, G., Moser, M., Müller, H., Pörtge, V., Risse, N., Roberts, G., Rosenburg, S., Röttenbacher, J., Schäfer, M., Schaefer, J., Schäfler, A., Schirmacher, I., Schneider, J., Schnitt, S., Stratmann, F., Tatzelt, C., Voigt, C., Walbröl, A., Weber, A., Wetzel, B., Wirth, 795 M., and Wendisch, M.: A comprehensive in-situ and remote sensing data set collected during the HALO–(AC)[3] aircraft campaign, Earth System Science Data Discussions, 2024, 1–49, https://doi.org/10.5194/essd-2024-281, 2024.

Ewald, F., Groß, S., Hagen, M., Hirsch, L., Delanoë, J., and Bauer-Pfundstein, M.: Calibration of a 35 GHz airborne cloud radar: lessons learned and intercomparisons with 94 GHz cloud radars, Atmospheric Measurement Techniques, 12, 1815–1839, https://doi.org/10.5194/amt-12-1815-2019, 2019.

800 Fearon, M. G., Doyle, J. D., Ryglicki, D. R., Finocchio, P. M., and Sprenger, M.: The Role of Cyclones in Moisture Transport into the Arctic, Geophysical Research Letters, 48, https://doi.org/10.1029/2020gl090353, 2021.

George, G., Stevens, B., Bony, S., Pincus, R., Fairall, C., Schulz, H., Kölling, T., Kalen, Q. T., Klingebiel, M., Konow, H., Lundry, A., Prange, M., and Radtke, J.: JOANNE: Joint dropsonde Observations of the Atmosphere in tropical North atlaNtic meso-scale Environments, Earth System Science Data, 13, 5253–5272, https://doi.org/10.5194/essd-13-5253-2021, 2021.

805 George, G., Luebke, A. E., Klingebiel, M., Mech, M., and Ehrlich, A.: Dropsonde measurements from HALO and POLAR 5 during HALO-$(\mathcal{AC})^3$ in 2022, https://doi.pangaea.de/10.1594/PANGAEA.968891, 2024.

Graham, R. M., Cohen, L., Ritzhaupt, N., Segger, B., Graversen, R. G., Rinke, A., Walden, V. P., Granskog, M. A., and Hudson, S. R.: Evaluation of Six Atmospheric Reanalyses over Arctic Sea Ice from Winter to Early Summer, Journal of Climate, 32, 4121–4143, https://doi.org/10.1175/jcli-d-18-0643.1, 2019.

810 Gray, W. R., Cluckie, I. D., and Griffith, R. J.: Aspects of melting and the radar bright band, Meteorological Applications, 8, 371–379, https://doi.org/10.1017/s1350482701003139, 2001.

Guan, B. and Waliser, D. E.: Detection of atmospheric rivers: Evaluation and application of an algorithm for global studies, Journal of Geophysical Research: Atmospheres, 120, 12 514–12 535, https://doi.org/10.1002/2015jd024257, 2015.

Guan, B. and Waliser, D. E.: Tracking Atmospheric Rivers Globally: Spatial Distributions and Temporal Evolution of Life Cycle Character- 815 istics, Journal of Geophysical Research: Atmospheres, 124, 12 523–12 552, https://doi.org/10.1029/2019jd031205, 2019.

Guan, B., Waliser, D. E., and Ralph, F. M.: A multimodel evaluation of the water vapor budget in atmospheric rivers, Annals of the New York Academy of Sciences, 1472, 139–154, https://doi.org/10.1111/nyas.14368, 2020.

Hersbach, H., Bell, B., Berrisford, P., Biavati, G., Horanyi, A., Sabater, J. M., Nicolas, J., Peubey, C., Radu, R., Rozum, I., Schepers, D., Simmons, A., Soci, C., Dee, D., and Thepaut, J.-N.: ERA5 hourly data on pressure levels from 1940 to present, Copernicus Climate 820 Change Service (C3S) Climate Data Store (CDS) [data set] (accessed 06-Feb-2024), https://doi.org/10.24381/cds.bd0915c6, 2018.

Hersbach, H., Bell, B., Berrisford, P., Hirahara, S., Nicolas, J., Peubey, C., Radu, R., Schepers, D., Simmons, A., Soci, C., Abdalla, S., Abellan, X., Balsamo, G., Bechtold, P., Biavati, G., Bidlot, J., Bonavita, M., Chiara, G., Dahlgren, P., Dee, D., Diamantakis, M., Dragani, R., Flemming, J., Forbes, R., Fuentes, M., Geer, A., Haimberger, L., Healy, S., Hogan, R. J., Keeley, S., Laloyaux, P., Lopez, P., Lupu,

C., Radnoti, G., Rosnay, P., Rozum, I., Vamborg, F., and Villaume, S.: The ERA5 global reanalysis, Quarterly Journal of the Royal Meteorological Society, 146, 1999–2049, https://doi.org/10.1002/qj.3803, 2020.

Heymsfield, A., Bansemer, A., Wood, N. B., Liu, G., Tanelli, S., Sy, O. O., Poellot, M., and Liu, C.: Toward Improving Ice Water Content and Snow-Rate Retrievals from Radars. Part II: Results from Three Wavelength Radar–Collocated In Situ Measurements and Cloud-Sat–GPM–TRMM Radar Data, Journal of Applied Meteorology and Climatology, 57, 365–389, https://doi.org/10.1175/jamc-d-17-0164.1, 2018.

Howland, M. R. and Sikdar, D. N.: The Moisture Budget over the Northeastern Arabian Sea during Premonsoon and Monsoon Onset, 1979, Monthly Weather Review, 111, 2255–2268, https://doi.org/10.1175/1520-0493(1983)111<2255:tmbotn>2.0.co;2, 1983.

Ignaccolo, M. and De Michele, C.: One, No One, and One Hundred Thousand: The Paradigm of the Z–R Relationship, Journal of Hydrometeorology, 21, 1161–1169, https://doi.org/10.1175/jhm-d-19-0177.1, 2020.

Illingworth, A. and Thompson, R.: Radar bright band correction using the linear depolarisation ratio, IAHS Publ. 3XX, 351, 2011.

Jacob, M., Ament, F., Gutleben, M., Konow, H., Mech, M., Wirth, M., and Crewell, S.: Investigating the liquid water path over the tropical Atlantic with synergistic airborne measurements, Atmospheric Measurement Techniques, 12, 3237–3254, https://doi.org/10.5194/amt-12-3237-2019, 2019.

Kirbus, B., Tiedeck, S., Camplani, A., Chylik, J., Crewell, S., Dahlke, S., Ebell, K., Gorodetskaya, I., Griesche, H., Handorf, D., Höschel, I., Lauer, M., Neggers, R., Rückert, J., Shupe, M. D., Spreen, G., Walbröl, A., Wendisch, M., and Rinke, A.: Surface impacts and associated mechanisms of a moisture intrusion into the Arctic observed in mid-April 2020 during MOSAiC, Frontiers in Earth Science, 11, https://doi.org/10.3389/feart.2023.1147848, 2023.

Kolbe, M., Sonnemans, J. P. J., Bintanja, R., van der Linden, E. C., van der Wiel, K., Whan, K., and Benedict, I.: Impact of Atmospheric Rivers on Future Poleward Moisture Transport and Arctic Climate in EC-Earth2, Journal of Geophysical Research: Atmospheres, 128, https://doi.org/10.1029/2023jd038926, 2023.

Komatsu, K. K., Alexeev, V. A., Repina, I. A., and Tachibana, Y.: Poleward upgliding Siberian atmospheric rivers over sea ice heat up Arctic upper air, Scientific Reports, 8, https://doi.org/10.1038/s41598-018-21159-6, 2018.

Konow, H., Jacob, M., Ament, F., Crewell, S., Ewald, F., Hagen, M., Hirsch, L., Jansen, F., Mech, M., and Stevens, B.: A unified data set of airborne cloud remote sensing using the HALO Microwave Package (HAMP), Earth System Science Data, 11, 921–934, https://doi.org/10.5194/essd-11-921-2019, 2019.

Konow, H., Ewald, F., George, G., Jacob, M., Klingebiel, M., Kölling, T., Luebke, A. E., Mieslinger, T., Pörtge, V., Radtke, J., Schäfer, M., Schulz, H., Vogel, R., Wirth, M., Bony, S., Crewell, S., Ehrlich, A., Forster, L., Giez, A., Gödde, F., Groß, S., Gutleben, M., Hagen, M., Hirsch, L., Jansen, F., Lang, T., Mayer, B., Mech, M., Prange, M., Schnitt, S., Vial, J., Walbröl, A., Wendisch, M., Wolf, K., Zinner, T., Zöger, M., Ament, F., and Stevens, B.: EUREC4A's HALO, Earth System Science Data, 13, 5545–5563, https://doi.org/10.5194/essd-13-5545-2021, 2021.

Lauer, M., Mech, M., and Guan, B.: Global Atmospheric Rivers catalog for ERA5 reanalysis [data set], https://doi.org/10.1594/PANGAEA.957161, 2023.

Lauer, M., Rinke, A., Gorodetskaya, I., Sprenger, M., Mech, M., and Crewell, S.: Influence of atmospheric rivers and associated weather systems on precipitation in the Arctic, Atmospheric Chemistry and Physics, 23, 8705–8726, https://doi.org/10.5194/acp-23-8705-2023, 2023.

Li, H. and Moisseev, D.: Melting Layer Attenuation at Ka- and W-Bands as Derived From Multifrequency Radar Doppler Spectra Observations, Journal of Geophysical Research: Atmospheres, 124, 9520–9533, https://doi.org/10.1029/2019jd030316, 2019.

Lin, Y.-L., Farley, R. D., and Orville, H. D.: Bulk Parameterization of the Snow Field in a Cloud Model, Journal of Climate and Applied Meteorology, 22, 1065–1092, https://doi.org/10.1175/1520-0450(1983)022<1065:bpotsf>2.0.co;2, 1983.

Ma, W., Chen, G., Peings, Y., and Alviz, N.: Atmospheric River Response to Arctic Sea Ice Loss in the Polar Amplification Model Intercomparison Project, Geophysical Research Letters, 48, https://doi.org/10.1029/2021gl094883, 2021.

Marshall, J. S. and Palmer, W. M. K.: THE DISTRIBUTION OF RAINDROPS WITH SIZE, Journal of Meteorology, 5, 165–166, https://doi.org/10.1175/1520-0469(1948)005<0165:tdorws>2.0.co;2, 1948.

Matrosov, S. Y.: Modeling Backscatter Properties of Snowfall at Millimeter Wavelengths, Journal of the Atmospheric Sciences, 64, 1727–1736, https://doi.org/10.1175/jas3904.1, 2007.

Mattingly, K. S., Mote, T. L., and Fettweis, X.: Atmospheric River Impacts on Greenland Ice Sheet Surface Mass Balance, JGR Atmospheres, 123, 8538–8560, https://doi.org/10.1029/2018jd028714, 2018.

Mech, M., Orlandi, E., Crewell, S., Ament, F., Hirsch, L., Hagen, M., Peters, G., and Stevens, B.: HAMP – the microwave package on the High Altitude and LOng range research aircraft (HALO), Atmospheric Measurement Techniques, 7, 4539–4553, https://doi.org/10.5194/amt-7-4539-2014, 2014.

Mech, M., Maahn, M., Kneifel, S., Ori, D., Orlandi, E., Kollias, P., Schemann, V., and Crewell, S.: PAMTRA 1.0: the Passive and Active Microwave radiative TRAnsfer tool for simulating radiometer and radar measurements of the cloudy atmosphere, Geoscientific Model Development, 13, 4229–4251, https://doi.org/10.5194/gmd-13-4229-2020, 2020.

Meneghini, R., Kim, H., Liao, L., Jones, J. A., and Kwiatkowski, J. M.: An Initial Assessment of the Surface Reference Technique Applied to Data from the Dual-Frequency Precipitation Radar (DPR) on the GPM Satellite, Journal of Atmospheric and Oceanic Technology, 32, 2281–2296, https://doi.org/10.1175/jtech-d-15-0044.1, 2015.

Nash, D., Waliser, D., Guan, B., Ye, H., and Ralph, F. M.: The Role of Atmospheric Rivers in Extratropical and Polar Hydroclimate, Journal of Geophysical Research: Atmospheres, 123, 6804–6821, https://doi.org/10.1029/2017jd028130, 2018.

Neff, W.: Atmospheric rivers melt Greenland, 8, 857–858, https://doi.org/10.1038/s41558-018-0297-4, 2018.

Neff, W., Compo, G. P., Ralph, F. M., and Shupe, M. D.: Continental heat anomalies and the extreme melting of the Greenland ice surface in 2012 and 1889, Journal of Geophysical Research: Atmospheres, 119, 6520–6536, https://doi.org/10.1002/2014jd021470, 2014.

Neiman, P. J., Wick, G. A., Moore, B. J., Ralph, F. M., Spackman, J. R., and Ward, B.: An Airborne Study of an Atmospheric River over the Subtropical Pacific during WISPAR: Dropsonde Budget-Box Diagnostics and Precipitation Impacts in Hawaii, Monthly Weather Review, 142, 3199–3223, https://doi.org/10.1175/mwr-d-13-00383.1, 2014.

Neiman, P. J., Moore, B. J., White, A. B., Wick, G. A., Aikins, J., Jackson, D. L., Spackman, J. R., and Ralph, F. M.: An Airborne and Ground-Based Study of a Long-Lived and Intense Atmospheric River with Mesoscale Frontal Waves Impacting California during CalWater-2014, Monthly Weather Review, 144, 1115–1144, https://doi.org/10.1175/mwr-d-15-0319.1, 2016.

Neiman, P. J., Gaggini, N., Fairall, C. W., Aikins, J., Spackman, J. R., Leung, L. R., Fan, J., Hardin, J., Nalli, N. R., and White, A. B.: An Analysis of Coordinated Observations from NOAA's Ronald H. Brown Ship and G-IV Aircraft in a Landfalling Atmospheric River over the North Pacific during CalWater-2015, Monthly Weather Review, 145, 3647–3669, https://doi.org/10.1175/mwr-d-17-0055.1, 2017.

Norris, J. R., Ralph, F. M., Demirdjian, R., Cannon, F., Blomquist, B., Fairall, C. W., Spackman, J. R., Tanelli, S., and Waliser, D. E.: The Observed Water Vapor Budget in an Atmospheric River over the Northeast Pacific, Journal of Hydrometeorology, 21, 2655–2673, https://doi.org/10.1175/jhm-d-20-0048.1, 2020.

Nygård, T., Naakka, T., and Vihma, T.: Horizontal Moisture Transport Dominates the Regional Moistening Patterns in the Arctic, Journal of Climate, 33, 6793–6807, https://doi.org/10.1175/jcli-d-19-0891.1, 2020.

900 Papritz, L., Aemisegger, F., and Wernli, H.: Sources and Transport Pathways of Precipitating Waters in Cold-Season Deep North Atlantic Cyclones, Journal of the Atmospheric Sciences, 78, 3349–3368, https://doi.org/10.1175/jas-d-21-0105.1, 2021.

Paulus, F. M., Karalis, M., George, G., Svensson, G., Wendisch, M., and Neggers, R. A. J.: Airborne measurements of mesoscale divergence at high latitudes during HALO-(AC)3, Journal of the Atmospheric Sciences, https://doi.org/10.1175/jas-d-24-0034.1, 2024.

Pithan, F., Svensson, G., Caballero, R., Chechin, D., Cronin, T. W., Ekman, A. M. L., Neggers, R., Shupe, M. D., Solomon, A., Tjernström,
905 M., and Wendisch, M.: Role of air-mass transformations in exchange between the Arctic and mid-latitudes, Nature Geosci, 11, 805–812, https://doi.org/10.1038/s41561-018-0234-1, 2018.

Ralph, F. M., Neiman, P. J., and Wick, G. A.: Satellite and CALJET Aircraft Observations of Atmospheric Rivers over the Eastern North Pacific Ocean during the Winter of 1997/98, Monthly Weather Review, 132, 1721–1745, https://doi.org/10.1175/1520-0493(2004)132<1721:sacaoo>2.0.co;2, 2004.

910 Ralph, F. M., Neiman, P. J., and Rotunno, R.: Dropsonde Observations in Low-Level Jets over the Northeastern Pacific Ocean from CALJET-1998 and PACJET-2001: Mean Vertical-Profile and Atmospheric-River Characteristics, 133, https://doi.org/10.1175/mwr2896.1, 2005.

Ralph, F. M., Iacobellis, S. F., Neiman, P. J., Cordeira, J. M., Spackman, J. R., Waliser, D. E., Wick, G. A., White, A. B., and Fairall, C.: Dropsonde Observations of Total Integrated Water Vapor Transport within North Pacific Atmospheric Rivers, Journal of Hydrometeorology, 18, 2577–2596, https://doi.org/10.1175/jhm-d-17-0036.1, 2017.

915 Rantanen, M., Karpechko, A. Y., Lipponen, A., Nordling, K., Hyvärinen, O., Ruosteenoja, K., Vihma, T., and Laaksonen, A.: The Arctic has warmed nearly four times faster than the globe since 1979, Communications Earth and Environment, 3, https://doi.org/10.1038/s43247-022-00498-3, 2022.

Rao, G. V., Schaub, W. R., and Puetz, J.: Evaporation and Precipitation over the Arabian Sea During Several Monsoon Seasons, Monthly Weather Review, 109, 364–370, https://doi.org/10.1175/1520-0493(1981)109<0364:eapota>2.0.co;2, 1981.

920 Rosenkranz, P. W.: Water vapor microwave continuum absorption: A comparison of measurements and models, Radio Science, 33, 919–928, https://doi.org/10.1029/98rs01182, 1998.

Sanders, F. and Gyakum, J. R.: Synoptic-Dynamic Climatology of the "Bomb", Monthly Weather Review, 108, 1589–1606, https://doi.org/10.1175/1520-0493(1980)108<1589:sdcot>2.0.co;2, 1980.

Schemann, V. and Ebell, K.: Simulation of mixed-phase clouds with the ICON large-eddy model in the complex Arctic environment around
925 Ny-Ålesund, Atmospheric Chemistry and Physics, 20, 475–485, https://doi.org/10.5194/acp-20-475-2020, 2020.

Schoger, S. Y., Moisseev, D., von Lerber, A., Crewell, S., and Ebell, K.: Snowfall-Rate Retrieval for K- and W-Band Radar Measurements Designed in Hyytiälä, Finland, and Tested at Ny-Ålesund, Svalbard, Norway, Journal of Applied Meteorology and Climatology, 60, 273–289, https://doi.org/10.1175/jamc-d-20-0095.1, 2021.

Schyberg, H., Yang, X., Koltzow, M., Amstrup, B., Bakketun, A., Bazile, E., Bojarova, J., Box, J. E., Dahlgren, P., Hagelin, S., Homleid,
930 M., Horanyi, A., Hoyer, J., Johansson, A., Killie, M., Koernich, H., Moigne, P. L., Lindskog, M., Manninen, T., Englyst, P. N., Nielsen, K., Olsson, E., Palmason, B., Aros, C. P., Randriamampianina, R., Samuelsson, P., Stappers, R., Stoylen, E., Thorsteinsson, S., Valkonen, T., and Wang, Z.: Arctic regional reanalysis on pressure levels from 1991 to present, Copernicus Climate Change Service (C3S) Climate Data Store(CDS) (accessed on 16-Jun-2022), https://doi.org/10.24381/CDS.E3C841AD, 2021.

Seager, R. and Henderson, N.: Diagnostic Computation of Moisture Budgets in the ERA-Interim Reanalysis with Reference to Analysis of
935 CMIP-Archived Atmospheric Model Data, Journal of Climate, 26, 7876–7901, https://doi.org/10.1175/jcli-d-13-00018.1, 2013.

Serreze, M. C. and Francis, J. A.: The Arctic Amplification Debate, Climatic Change, 76, 241–264, https://doi.org/10.1007/s10584-005-9017-y, 2006.

Spreen, G., Kaleschke, L., and Heygster, G.: Sea ice remote sensing using AMSR-E 89-GHz channels, Journal of Geophysical Research: Oceans, 113, https://doi.org/10.1029/2005jc003384, 2008.

940 Stevens, B., Ament, F., Bony, S., Crewell, S., Ewald, F., Gross, S., Hansen, A., Hirsch, L., Jacob, M., Kölling, T., Konow, H., Mayer, B., Wendisch, M., Wirth, M., Wolf, K., Bakan, S., Bauer-Pfundstein, M., Brueck, M., Delanoë, J., Ehrlich, A., Farrell, D., Forde, M., Gödde, F., Grob, H., Hagen, M., Jäkel, E., Jansen, F., Klepp, C., Klingebiel, M., Mech, M., Peters, G., Rapp, M., Wing, A. A., and Zinner, T.: A High-Altitude Long-Range Aircraft Configured as a Cloud Observatory: The NARVAL Expeditions, Bulletin of the American Meteorological Society, 100, 1061–1077, https://doi.org/10.1175/bams-d-18-0198.1, 2019.

945 Vaisala: Vaisala Radiosonde RD41 datasheet in English, B211706EN-B, https://www.nirb.ca/portal/dms/script/dms_download.php?fileid= 1215340414&applicationid=125718&sessionid=ka7asjkahsplnt1tq4rduoqbl1, 2020.

Vaquero-Martínez, J., Antón, M., Román, R., Cachorro, V. E., Wang, H., González Abad, G., and Ritter, C.: Water vapor satellite products in the European Arctic: An inter-comparison against GNSS data, Science of The Total Environment, 741, 140 335, https://doi.org/10.1016/j.scitotenv.2020.140335, 2020.

950 Vázquez, M., Algarra, I., Eiras-Barca, J., Ramos, A. M., Nieto, R., and Gimeno, L.: Atmospheric Rivers over the Arctic: Lagrangian Characterisation of Their Moisture Sources, Water, 11, 41, https://doi.org/10.3390/w11010041, 2018.

Viceto, C., Gorodetskaya, I. V., Rinke, A., Maturilli, M., Rocha, A., and Crewell, S.: Atmospheric rivers and associated precipitation patterns during the ACLOUD and PASCAL campaigns near Svalbard (May–June 2017): case studies using observations, reanalyses, and a regional climate model, Atmospheric Chemistry and Physics, 22, 441–463, https://doi.org/10.5194/acp-22-441-2022, 2022.

955 Walbröl, A., Michaelis, J., Becker, S., Dorff, H., Ebell, K., Gorodetskaya, I., Heinold, B., Kirbus, B., Lauer, M., Maherndl, N., Maturilli, M., Mayer, J., Müller, H., Neggers, R. A. J., Paulus, F. M., Röttenbacher, J., Rückert, J. E., Schirmacher, I., Slättberg, N., Ehrlich, A., Wendisch, M., and Crewell, S.: Contrasting extremely warm and long-lasting cold air anomalies in the North Atlantic sector of the Arctic during the HALO-(AC)[3] campaign, Atmospheric Chemistry and Physics, 24, 8007–8029, https://doi.org/10.5194/acp-24-8007-2024, 2024.

Wang, C., Graham, R. M., Wang, K., Gerland, S., and Granskog, M. A.: Comparison of ERA5 and ERA-Interim near-surface air temperature, 960 snowfall and precipitation over Arctic sea ice: effects on sea ice thermodynamics and evolution, The Cryosphere, 13, 1661–1679, https://doi.org/10.5194/tc-13-1661-2019, 2019.

Wendisch, M., Handorf, D., Tegen, I., Neggers, R., and Spreen, G.: Glimpsing the Ins and Outs of the Arctic Atmospheric Cauldron, Eos, 102, https://doi.org/10.1029/2021eo155959, 2021.

Wendisch, M., Brückner, M., Crewell, S., Ehrlich, A., Notholt, J., Lüpkes, C., Macke, A., Burrows, J. P., Rinke, A., Quaas, J., Maturilli, 965 M., Schemann, V., Shupe, M. D., Akansu, E. F., Barrientos-Velasco, C., Bärfuss, K., Blechschmidt, A.-M., Block, K., Bougoudis, I., Bozem, H., Böckmann, C., Bracher, A., Bresson, H., Bretschneider, L., Buschmann, M., Chechin, D. G., Chylik, J., Dahlke, S., Deneke, H., Dethloff, K., Donth, T., Dorn, W., Dupuy, R., Ebell, K., Egerer, U., Engelmann, R., Eppers, O., Gerdes, R., Gierens, R., Gorodetskaya, I. V., Gottschalk, M., Griesche, H., Gryanik, V. M., Handorf, D., Harm-Altstädter, B., Hartmann, J., Hartmann, M., Heinold, B., Herber, A., Herrmann, H., Heygster, G., Höschel, I., Hofmann, Z., Hölemann, J., Hünerbein, A., Jafariserajehlou, S., Jäkel, E., Jacobi, C., Janout, 970 M., Jansen, F., Jourdan, O., Jurányi, Z., Kalesse-Los, H., Kanzow, T., Käthner, R., Kliesch, L. L., Klingebiel, M., Knudsen, E. M., Kovács, T., Körtke, W., Krampe, D., Kretzschmar, J., Kreyling, D., Kulla, B., Kunkel, D., Lampert, A., Lauer, M., Lelli, L., von Lerber, A., Linke, O., Löhnert, U., Lonardi, M., Losa, S. N., Losch, M., Maahn, M., Mech, M., Mei, L., Mertes, S., Metzner, E., Mewes, D., Michaelis, J., Mioche, G., Moser, M., Nakoudi, K., Neggers, R., Neuber, R., Nomokonova, T., Oelker, J., Papakonstantinou-Presvelou, I., Pätzold, F., Pefanis, V., Pohl, C., van Pinxteren, M., Radovan, A., Rhein, M., Rex, M., Richter, A., Risse, N., Ritter, C., Rostosky, P., Rozanov, V. V., 975 Donoso, E. R., Saavedra Garfias, P., Salzmann, M., Schacht, J., Schäfer, M., Schneider, J., Schnierstein, N., Seifert, P., Seo, S., Siebert,

H., Soppa, M. A., Spreen, G., Stachlewska, I. S., Stapf, J., Stratmann, F., Tegen, I., Viceto, C., Voigt, C., Vountas, M., Walbröl, A., Walter, M., Wehner, B., Wex, H., Willmes, S., Zanatta, M., and Zeppenfeld, S.: Atmospheric and Surface Processes, and Feedback Mechanisms Determining Arctic Amplification: A Review of First Results and Prospects of the (AC)3 Project, Bulletin of the American Meteorological Society, 104, E208–E242, https://doi.org/10.1175/bams-d-21-0218.1, 2023.

980   Wendisch, M., Crewell, S., Ehrlich, A., Herber, A., Kirbus, B., Lüpkes, C., Mech, M., Abel, S. J., Akansu, E. F., Ament, F., Aubry, C., Becker, S., Borrmann, S., Bozem, H., Brückner, M., Clemen, H.-C., Dahlke, S., Dekoutsidis, G., Delanoë, J., De La Torre Castro, E., Dorff, H., Dupuy, R., Eppers, O., Ewald, F., George, G., Gorodetskaya, I. V., Grawe, S., Groß, S., Hartmann, J., Henning, S., Hirsch, L., Jäkel, E., Joppe, P., Jourdan, O., Jurányi, Z., Karalis, M., Kellermann, M., Klingebiel, M., Lonardi, M., Lucke, J., Luebke, A. E., Maahn, M., Maherndl, N., Maturilli, M., Mayer, B., Mayer, J., Mertes, S., Michaelis, J., Michalkov, M., Mioche, G., Moser, M., Müller, H., Neggers,

985   R., Ori, D., Paul, D., Paulus, F. M., Pilz, C., Pithan, F., Pöhlker, M., Pörtge, V., Ringel, M., Risse, N., Roberts, G. C., Rosenburg, S., Röttenbacher, J., Rückert, J., Schäfer, M., Schaefer, J., Schemann, V., Schirmacher, I., Schmidt, J., Schmidt, S., Schneider, J., Schnitt, S., Schwarz, A., Siebert, H., Sodemann, H., Sperzel, T., Spreen, G., Stevens, B., Stratmann, F., Svensson, G., Tatzelt, C., Tuch, T., Vihma, T., Voigt, C., Volkmer, L., Walbröl, A., Weber, A., Wehner, B., Wetzel, B., Wirth, M., and Zinner, T.: Overview: quasi-Lagrangian observations of Arctic air mass transformations – introduction and initial results of the HALO–$(\mathcal{AC})^3$ aircraft campaign, Atmospheric Chemistry and

990   Physics, 24, 8865–8892, https://doi.org/10.5194/acp-24-8865-2024, 2024.

Wesche, C., Steinhage, D., and Nixdorf, U.: Polar aircraft Polar5 and Polar6 operated by the Alfred Wegener Institute, Journal of large-scale research facilities JLSRF, 2, A87, https://doi.org/10.17815/jlsrf-2-153, 2016.

Wong, S., Genio, A. D. D., Wang, T., Kahn, B. H., Fetzer, E. J., and L'Ecuyer, T. S.: Responses of Tropical Ocean Clouds and Precipitation to the Large-Scale Circulation: Atmospheric-Water-Budget-Related Phase Space and Dynamical Regimes, Journal of Climate, 29, 7127–

995   7143, https://doi.org/10.1175/jcli-d-15-0712.1, 2016.

Woods, C. and Caballero, R.: The Role of Moist Intrusions in Winter Arctic Warming and Sea Ice Decline, Journal of Climate, 29, 4473–4485, https://doi.org/10.1175/jcli-d-15-0773.1, 2016.

Wu, H., Xu, X., Luo, T., Yang, Y., Xiong, Z., and Wang, Y.: Variation and comparison of cloud cover in MODIS and four reanalysis datasets of ERA-interim, ERA5, MERRA-2 and NCEP, Atmospheric Research, 281, https://doi.org/10.1016/j.atmosres.2022.106477, 2023.

1000 You, C., Tjernström, M., and Devasthale, A.: Warm and moist air intrusions into the winter Arctic: a Lagrangian view on the near-surface energy budgets, Atmospheric Chemistry and Physics, 22, 8037–8057, https://doi.org/10.5194/acp-22-8037-2022, 2022.

Zabolotskikh, E. and Azarov, S.: Wintertime Emissivities of the Arctic Sea Ice Types at the AMSR2 Frequencies, Remote Sensing, 14, 5927, https://doi.org/10.3390/rs14235927, 2022.

Zängl, G., Reinert, D., Rípodas, P., and Baldauf, M.: The ICON (ICOsahedral Non-hydrostatic) modelling framework of DWD and

1005 MPI-M: Description of the non-hydrostatic dynamical core, Quarterly Journal of the Royal Meteorological Society, 141, 563–579, https://doi.org/10.1002/qj.2378, 2014.

Zhang, C., Tung, W.-W., and Cleveland, W. S.: Atlas of Arctic Atmospheric River Climatology Based on ERA5 and MERRA-2, https://doi.org/10.1002/essoar.10511981.1, 2022.

Zhang, P., Chen, G., Ting, M., Ruby Leung, L., Guan, B., and Li, L.: More frequent atmospheric rivers slow the seasonal recovery of Arctic

1010 sea ice, Nature Climate Change, 13, 266–273, https://doi.org/10.1038/s41558-023-01599-3, 2023.

Zhu, Y. and Newell, R. E.: A Proposed Algorithm for Moisture Fluxes from Atmospheric Rivers, Monthly Weather Review, 126, 725–735, https://doi.org/10.1175/1520-0493(1998)126<0725:apafmf>2.0.co;2, 1998.